JGR Space Physics

RESEARCH ARTICLE
10.1029/2024JA032887

The Spatial Variation of Large- and Meso-Scale Plasma Flow Vorticity Statistics in the High-Latitude Ionosphere and Implications for Ionospheric Plasma Flow Models

G. Chisham[1] and **M. P. Freeman**[1]

[1]British Antarctic Survey, Cambridge, UK

Key Points:

- The spatial variation of meso-scale ionospheric flow vorticity is independent of the prevailing IMF B_y direction
- Meso-scale ionospheric flow vorticity is strongest in the cusp and the auroral region
- Meso-scale ionospheric flow vorticity is most intermittent in the polar cap and the sub-auroral region

Correspondence to:
G. Chisham,
gchi@bas.ac.uk

Citation:
Chisham, G., & Freeman, M. P. (2024). The spatial variation of large- and meso-scale plasma flow vorticity statistics in the high-latitude ionosphere and implications for ionospheric plasma flow models. *Journal of Geophysical Research: Space Physics*, *129*, e2024JA032887. https://doi.org/10.1029/2024JA032887

Received 16 MAY 2024
Accepted 15 JUL 2024

Author Contributions:
Conceptualization: G. Chisham, M. P. Freeman
Formal analysis: G. Chisham
Investigation: G. Chisham, M. P. Freeman
Methodology: G. Chisham
Project administration: M. P. Freeman
Software: G. Chisham
Visualization: G. Chisham
Writing – original draft: G. Chisham
Writing – review & editing: G. Chisham, M. P. Freeman

Abstract The ability to understand and model ionospheric plasma flow on all spatial scales has important implications for operational space weather models. This study exploits a recently developed method to statistically separate large-scale and meso-scale contributions to probability density functions (PDFs) of ionospheric flow vorticity measured by the Super Dual Auroral Radar Network (SuperDARN). The SuperDARN vorticity data are first sub-divided depending on the Interplanetary Magnetic Field (IMF) direction, and the separation method is applied to PDFs of vorticity compiled in spatial regions of size 1° of geomagnetic latitude by 1 hr of magnetic local time, covering much of the high-latitude ionosphere in the northern hemisphere. The resulting PDFs are fit by model functions using maximum likelihood estimation (MLE) and the spatial variations of the MLE estimators for both the large-scale and meso-scale components are presented. The spatial variations of the large-scale vorticity estimators are ordered by the average ionospheric convection flow, which is highly dependent on the IMF direction. The spatial variations of the meso-scale vorticity estimators appear independent of the senses of vorticity and IMF direction, but have a different character in the polar cap, the cusp, the auroral region, and the sub-auroral region. The paper concludes by discussing the sources of the vorticity components in the different regions, and the consequences for the fidelity of ionospheric plasma flow models.

Plain Language Summary The ability to accurately model the flow of ionized gases (plasma) in the Earth's ionosphere (the ionized region of the Earth's upper atmosphere) has important implications for operational space weather models. Large-scale variations in this plasma flow are modeled well, but fluctuations on the meso-scale and small scale are typically ignored in these models. This study uses measurements from a high-latitude ground-based radar network to measure the ionospheric plasma flow in terms of its vorticity (how straight or curved the flow is). The measured vorticity is separated into components related to both the large and meso-scale fluctuations. The paper discusses the origins of the meso-scale component, and what needs to be done before it can be confidently added to ionospheric plasma flow models.

1. Introduction

The ability to accurately measure and model ionospheric plasma flow and its associated electric field is becoming increasingly important for space weather applications (Lam et al., 2023; Liu et al., 2018; Orr et al., 2023). Flow measurements and models are necessary for estimating Joule heating (Billett et al., 2018; Kalafatoglu Eyiguler et al., 2018; Weimer, 2005), which is a key influence affecting the atmospheric drag on low-Earth orbit satellites (Bruinsma et al., 2023; Fedrizzi et al., 2012). They are also required to predict the motion of patches of enhanced ionization in the polar cap (Eriksen et al., 2023; Fæhn Follestad et al., 2019; Zhang et al., 2013), which can result in the disruption of GNSS (Global Navigation Satellite System) signals from spacecraft (van der Meeren et al., 2015; Zhang et al., 2017).

The large-scale (~1,000 km) nature of ionospheric plasma flow is very well understood. The flow strength is controlled by the magnetic reconnection rates at the Earth's magnetopause and in the magnetotail (Chisham et al., 2008; Dungey, 1961). The size of the flow pattern is determined by the differences between dayside and nightside reconnection, and the spatial patterns of ionospheric flow depend on the Interplanetary Magnetic Field (IMF) direction (Cowley & Lockwood, 1992; Lockwood et al., 1990; Milan et al., 2012; Siscoe & Huang, 1985). Ionospheric measurements of the large-scale plasma flow can in fact be used to estimate the rates of this magnetic reconnection (Chisham et al., 2008; Hubert et al., 2006; Milan et al., 2003).

The last few decades have seen the development of empirical climatological models of the large-scale ionospheric plasma flow and its associated electric field in which the average measured flow is found at a given location for a solar wind state and time of year. These models have exploited ionospheric plasma flow measurements from a wide range of instrumentation, including incoherent scatter radar (Foster, 1983), coherent scatter radar (Pettigrew et al., 2010; Ruohoniemi & Greenwald, 2005; Thomas & Shepherd, 2018), low-altitude spacecraft (Hairston & Heelis, 1990; Weimer, 2001, 2005), high-altitude spacecraft (Förster et al., 2007), and ground-based magnetometers (Ridley et al., 2000). Somewhat differently, a solar-cycle Empirical Orthogonal Function (EOF) reanalysis of ionospheric flow data measured by the Super Dual Auroral Radar Network (SuperDARN) (Shore et al., 2021) has been exploited to develop a regression model of the ionospheric plasma flow, based on only a few solar wind input parameters (Lam et al., 2023). Continuous observations from ground-based networks of coherent scatter radars, such as SuperDARN, have also been assimilated into climatological models to improve their estimation of the large-scale ionospheric plasma flow across the polar regions (Ruohoniemi & Baker, 1998).

Like the large-scale flow, some meso-scale (∼100 km) and small-scale (<∼1–10 km) variations in the ionospheric plasma flow can also be causally related to magnetic reconnection or other solar wind-magnetosphere interactions. For example, meso-scale vortical flows called Traveling Convection Vortices (TCVs) (Friis-Christensen et al., 1988; Glassmeier & Heppner, 1992; Lyatsky et al., 1999), are driven by pressure variations in the solar wind impacting the magnetosphere. Other transient meso-scale flow phenomena in the ionospheric cusp region have been shown to be the ionospheric signatures of flux transfer events (FTEs) at the magnetopause (Russell & Elphic, 1979). Some of these events have been observed to have a vorticity sense that is the same as the background flow (so-called 'Flow Channel Events' or 'Pulsed Ionospheric Flows') (Chisham et al., 2000; Oksavik et al., 2004; Pinnock et al., 1993; Provan et al., 1998), whereas for others the vorticity sense is opposite to the background flow (so-called 'Reverse Flow Events' - RFEs) (Moen et al., 2008; Oksavik et al., 2011; Rinne et al., 2007; Spicher et al., 2016). More generally, meso-scale and small-scale flow variations are not deterministic and need to be studied through statistical analyses across scales within the framework of MHD turbulence (Abel et al., 2006, 2007, 2009; Chaston et al., 2008; Di Mare et al., 2021; Kintner & Seyler, 1985; Spicher et al., 2015). Small-scale fluctuations are often associated with meso-scale variations in the flow, occurring in the region of flow shears in the auroral oval (Basu et al., 1988) and cusp (Carlson et al., 2007).

Global ionospheric flow models have not yet adequately incorporated meso-scale and small-scale flow variations. Determining the most appropriate model of turbulence for meso-scale ionospheric flow measured by SuperDARN has been attempted (Abel et al., 2006, 2007, 2009), but is complicated by the sensitivity of the model to rare extreme fluctuations that are hard to measure. The results suggest a Kraichnan-Iroshnikov (K-I) model, whose intermittency varies with location and IMF direction, but more work is needed to understand the spatial variation of turbulent fluctuations. In turbulence, vorticity cascades from the large to meso to small scales, and thus measurements of the vorticity in fluid flow are useful (Chorin, 2013). K-I turbulence requires two-dimensional measurements of the fluid flow, but standard global two-dimensional representations of ionospheric plasma flow are limited to the large-scale variations (Ruohoniemi & Baker, 1998). However, methods have been developed to locally measure vorticity in SuperDARN measurements of ionospheric plasma flow (Chisham et al., 2009; Sofko et al., 1995), by measuring the flow around closed loops defined by the look directions of overlapping radar fields-of-view, and exploiting Stokes' theorem. This has enabled the study of ionospheric flow vorticity on both the large and meso-scale, though small-scale measurement remains elusive with this instrumentation due to the typical 45 km range gate resolution of the SuperDARN radars.

Compilation of probability density functions (PDFs) of SuperDARN flow vorticity measurements, has improved our understanding of the nature of meso-scale flow variations in the northern hemisphere high-latitude region. These PDFs have been shown to be highly leptokurtic (higher kurtosis than a Gaussian) (Chisham & Freeman, 2010), and their distribution shape and scale shown to vary with location and IMF direction (Chisham & Freeman, 2021, 2023), qualitatively consistent with the results of Abel et al. (2006, 2007, 2009). The spatial variation of the PDF shape and scale was shown to be ordered by the large-scale flow vorticity and the magnetic field-aligned current (FAC) systems that couple the magnetosphere to the high-latitude ionosphere (FAC is proportional to vorticity in the limit of uniform ionospheric conductance). Coxon et al. (2022, 2023) have shown that PDFs of FACs measured in the ionosphere are similarly leptokurtic, with a similar spatial variation in distribution shape and scale to the flow vorticity.

Recently, Chisham and Freeman (2023) developed a new method to statistically separate the contributions of large and meso-scale variations in the measured flow vorticity PDFs. Their results suggested that there are regions of the high-latitude ionosphere where the effects of meso-scale vorticity outweigh those of the large-scale vorticity. Hence, in these regions, present ionospheric flow models are severely lacking. However, Chisham and Freeman (2023) only determined the separation of these components in two small high-latitude regions, to illustrate the potential of the methodology. In this paper, we extend this method to almost the whole of the northern hemisphere high-latitude region in order to study the spatial variation of these two vorticity components. As in Chisham and Freeman (2010, 2021, 2023), we use maximum likelihood estimation (MLE) to fit model functions to the PDFs at each location.

The paper is structured as follows. Section 2 presents the methodology, including details of the measurement of ionospheric plasma flow vorticity and the compilation of the PDFs, an outline of the methodology used for the separation of the vorticity PDFs into large-scale and meso-scale components, the methods used to model the observed PDFs using MLE, and examples of the PDF component separation and the MLE model fitting. Section 3 presents the results of the analyses, showing the spatial variation of the MLE fit estimators across the high-latitude ionosphere for both the large-scale and meso-scale vorticity components, for IMF B_y positive and IMF B_y negative conditions. Section 4 discusses the observations, speculates about the causes of the observed spatial variation in the plasma flow vorticity, and discusses how meso-scale fluctuations could be introduced into models. Section 5 summarizes and concludes the paper. Henceforth, all references to vorticity in the paper refer to the vorticity of the ionospheric plasma flow.

2. Methodology

2.1. Ionospheric Vorticity Determination

This study uses estimates of ionospheric plasma flow vorticity derived from line-of-sight Doppler velocity measurements of plasma flow from SuperDARN. SuperDARN (Chisham et al., 2007; Greenwald et al., 1995; Nishitani et al., 2019) is a ground-based network of over 30 High Frequency (HF) radars that can measure plasma flow variations in the mid- and high-latitude ionosphere in both hemispheres. The radars transmit HF radio signals in the range 8–20 MHz that are backscattered by magnetic field-aligned density irregularities in the F-region ionosphere and received back at the radars (Greenwald et al., 1985). These irregularities move with the background ionospheric plasma flow (Villain et al., 1985), allowing the line-of-sight component of the flow to be estimated from the Doppler shift of the received signal. The SuperDARN radars typically transmit in narrow beams (of typical width ∼3.25°) (Greenwald et al., 1985) and typically sample at ∼70 to 150 range gates of size 45 km along the beams. The radars typically scan along 16 to 24 beam directions over an interval of 1-min, covering an azimuthal area of ∼52°–78° (Nishitani et al., 2019).

Chisham et al. (2009) developed a method to derive magnetic field-aligned ionospheric plasma flow vorticity from line-of-sight Doppler velocity measurements from SuperDARN radars with overlapping fields of view; the method has many similarities with that proposed earlier by Sofko et al. (1995) in that they both use Stokes' theorem to determine vorticity from measurements of the flow around closed loops. Full details of this technique can be found in Chisham et al. (2009) and more concise descriptions in Chisham and Freeman (2010, 2021, 2023). The vorticity data set used in this study (Chisham, 2023) covers the interval 2000–2005 inclusive, as used previously by Chisham and Freeman (2021, 2023). In this data set, a positive field-aligned vorticity relates to a clockwise rotation when looking in the direction of the magnetic field into the northern hemisphere ionosphere, and a negative field-aligned vorticity relates to an anti-clockwise rotation.

The vorticity data used in this study are separated by the prevailing IMF conditions. We use the vorticity data from two sub-groups defined by the IMF clock angle in the Geocentric Solar Magnetospheric (GSM) *Y-Z* plane. These two sub-groups are of size 45° in clock angle centered on the IMF B_y positive and IMF B_y negative directions, which were previously shown to have significantly different influences on the vorticity PDFs (Chisham & Freeman, 2023). We use IMF data for the interval from OMNIWeb, which is lagged from the spacecraft to the Earth's bow shock. We restrict our analysis to stable IMF intervals, defined by 30-min intervals within which 70% of the measured clock angle values are within the same bin, as described in Chisham et al. (2009). As well as being separated by the prevailing IMF conditions, the vorticity data are separated by their spatial location in the Altitude-Adjusted Corrected GeoMagnetic (AACGM) latitude and Magnetic Local Time (MLT) co-ordinate system (Shepherd, 2014).

The vorticity PDFs are compiled in the following way: The PDF value ($f(\omega_i, x_j)$) for any vorticity bin ω_i and location bin x_j is given by,

$$f(\omega_i, x_j) = \frac{n(\omega_i, x_j)}{N(x_j)\,W}, \tag{1}$$

where $n(\omega_i, x_j)$ is the number of vorticity values in vorticity bin ω_i at location x_j,

$$N(x_j) = \sum_i n(\omega_i, x_j), \tag{2}$$

is the total number of vorticity values in all vorticity bins at location x_j, and W is the vorticity bin width; we use $W = 1$ mHz in this study, as in Chisham and Freeman (2021, 2023). The PDF uncertainty in each bin is given by,

$$\sigma(\omega_i, x_j) = \frac{\sqrt{n(\omega_i, x_j)}}{N(x_j)\,W}. \tag{3}$$

Chisham and Freeman (2023) only studied the PDFs measured in 4 small spatial regions which most strongly demonstrated the IMF B_y influence; here, the 6 years of vorticity measurements are subdivided into smaller spatial bins of size 1° of AACGM latitude by 1-hr of MLT, covering much of the northern hemisphere high-latitude ionosphere. Vorticity PDFs are determined for every spatial bin, for both IMF subgroups.

2.2. Separation of PDF Components

Ionospheric vorticity PDFs presented in previous papers have been shown to be typically asymmetric (Chisham & Freeman, 2021, 2023). Hence, these studies have analyzed the positive and negative vorticity portions of the PDFs independently. From a comparison of the PDFs observed during opposing IMF B_y conditions, Chisham and Freeman (2023) concluded that this asymmetry was a result of different combinations of the 'large-scale' (LS) vorticity inherent in the ionospheric convection driven by magnetic reconnection, and the 'meso-scale' (MS) vorticity associated with fluid processes, such as turbulence, and measurement errors.

Chisham and Freeman (2023) separated the different contributions to the vorticity PDFs by making the following assumptions.

1. On the spatial scales of the individual PDFs, the MS component is symmetric around zero (i.e., there is no preferred sense to the MS vorticity in a single measurement cell).
2. On the spatial scales of the individual PDFs, the LS component is single-sided (i.e., there is only a single sense to the LS vorticity direction in a single measurement cell).

Following these assumptions, the two sides of the measured vorticity PDF at any location were treated in the following way. The side with the lower number of observed vorticity values was assumed to contain wholly MS vorticity values. These PDFs were always leptokurtic, and the vorticity data on this side of the PDF were fit with a q-exponential distribution using MLE. The q-exponential has been shown to be a good model for ionospheric vorticity (Chisham & Freeman, 2010, 2021, 2023), as well as for fluctuations in other space plasmas (Burlaga et al., 2007; Esquivel & Lazarian, 2010). On the side with the higher number of observed vorticity values the MS component of the PDF was assumed to be the same as the opposite side with the lower number, and the LS component of the PDF was determined by subtracting the mirrored MS PDF values from the total measured PDF values. Following the theoretical arguments presented in Chisham and Freeman (2010), Chisham and Freeman (2023) decided that the LS vorticity PDFs would be better modeled by a single-sided Weibull function. As this LS component was only characterized by the binned PDF values, Chisham and Freeman (2023) fitted the Weibull function to the binned LS PDF by eye rather than using MLE.

Although these model distributions fitted very well to the observed vorticity PDFs, this 'fit-by-eye' method is not practical for the more extensive analysis of the PDFs in multiple locations that is employed in this study. Fitting using MLE is a much more accurate process as it uses all the individual vorticity measurements rather than solely the binned PDF values. To facilitate MLE of the model parameters we use an automated algorithm for the PDF separation as outlined below. This methodology is opposite depending on which side of the PDF contains the most vorticity measurements. Here, we only outline the case where

$$N_{-}(x_j) > N_{+}(x_j), \tag{4}$$

where $N_{-}(x_j)$ represents the number of vorticity measurements in all the negative vorticity bins ($\sum n_{-}(\omega_i, x_j)$), and $N_{+}(x_j)$ represents the number of vorticity measurements in all the positive vorticity bins ($\sum n_{+}(\omega_i, x_j)$). For this analysis, we have to separate the observed negative vorticity data into the two separate MS and LS populations that can then be fit with the different model distributions using MLE. For this separation we use the following probability to estimate whether any individual measured vorticity value ω in the ω_i bin ($\omega \in \omega_i$) is likely to be part of the LS distribution. Otherwise, it is assumed to be part of the MS distribution.

We assess that the probability of any measured vorticity value ω being part of the LS distribution can be approximated by,

$$P_{LS}(\omega \in \omega_i, x_j) = \frac{(n_{-}(\omega_i, x_j) + \epsilon_{n-}(\omega_i, x_j)) - (n_{+}(\omega_i, x_j) + \epsilon_{n+}(\omega_i, x_j))}{n_{-}(\omega_i, x_j)}, \tag{5}$$

where the terms

$$\epsilon_{n+}(\omega_i, x_j) \in_R \Phi\left(0, \sqrt{n_{+}(\omega_i, x_j)}\right), \tag{6}$$

and,

$$\epsilon_{n-}(\omega_i, x_j) \in_R \Phi\left(0, \sqrt{n_{-}(\omega_i, x_j)}\right). \tag{7}$$

are random numbers selected from a normal distribution of mean 0 and standard deviation $\sqrt{n(\omega_i, x_j)}$ to take into account the statistical uncertainties in the measured vorticity occurrence numbers ($n(\omega_i, x_j)$) in each PDF bin. To select the population into which this vorticity value ω is placed, we determine a random number R_ω between 0 and 1. If $R_\omega \leq P_{LS}$ then the vorticity value is assumed to be part of the LS vorticity population. If $R_\omega > P_{LS}$ then the vorticity value is assumed to be part of the MS vorticity population.

This analysis results in two separate vorticity populations for negative vorticity for which the binned PDF values are $f_{LS}(\omega_i, x_j)$ and $f_{MS}(\omega_i, x_j)$, whereas positive vorticity is characterized by a single population and PDF that includes all the measured positive vorticity values. The same equations are used for the case where there are a larger number of positive vorticity measurements ($N_{+}(x_j) > N_{-}(x_j)$), but with the signs for n reversed.

2.3. Model Fitting of PDFs

Following the methods used by Chisham and Freeman (2010, 2021, 2023), we use MLE to model the measured ionospheric vorticity PDFs. The MS vorticity populations are modeled by q-exponential distributions of the form

$$f_{q,\kappa}(\omega) = \frac{1}{\kappa}\left(1 - \frac{(1-q)\omega}{\kappa}\right)^{q/(1-q)} \tag{8}$$

using the MLE method outlined in Shalizi (2007). Here, q and κ are the parameters that define the distribution, and we use $\hat{q}$ and $\hat{\kappa}$ as their maximum likelihood estimators. In q-exponential distributions, q describes the distribution

shape whereas κ describes the distribution scale. The q-exponential distributions tend toward exponential as q tends toward 1 and become increasingly heavy-tailed as q increases greater than 1.

The LS vorticity populations are modeled by Weibull distributions of the form,

$$f_{c,\chi}(\omega) = \frac{c}{\chi}\left(\frac{\omega}{\chi}\right)^{c-1} \exp\left[-\left(\frac{\omega}{\chi}\right)^{c}\right] \tag{9}$$

using the MLE method of Qiao and Tsokos (1994), where c and χ represent the shape and scale parameters, respectively, and where the function becomes an exponential when c equals 1. We use $\hat{c}$ and $\hat{\chi}$ as their maximum likelihood estimators.

Owing to the smaller area of the spatial bins used in this study, the typical number of vorticity values measured in any particular spatial bin is reduced compared to Chisham and Freeman (2023). In previous studies (Chisham & Freeman, 2010, 2021, 2023), we assumed that at least $N = 100$ vorticity values are required for an accurate MLE determination of the q-exponential and Weibull estimators but presented no assessment of how the level of uncertainty in the estimators varied with N. To address this, we simulate a large number of q-exponential and Weibull samples with different occurrence numbers, apply the MLE process, and assess the accuracy of the estimators. Specifically, we select sample sizes ranging from $N = 10$ to 10,000 points in equally spaced intervals in logarithmic space. For each N, we simulate 1,000 different samples by randomly sampling either a q-exponential distribution with fixed q and κ, or a Weibull distribution with fixed c and χ. From these 1,000 samples we determine the median and interquartile range of the MLE estimators $\hat{q}$ and $\hat{\kappa}$, or $\hat{c}$ and $\hat{\chi}$, depending on the parent distribution.

Figures 1a and 1b present the results of these simulations for two fixed sets of q-exponential parameters typical of the ionospheric vorticity PDFs measured in this paper; $q = 1.4$ and $\kappa = 0.0005$ (red), and $q = 1.05$ and $\kappa = 0.0025$ (black). The square symbols represent the median values of the estimators from the 1,000 simulated samples, and the vertical lines mark the extent of their interquartile range. The horizontal dashed lines represent the expected values. As the simulated sample size increases toward $N = 10{,}000$, the MLE estimators become increasingly well defined, with the median values matching those expected, and with increasingly smaller interquartile ranges. As the sample size decreases toward $N = 10$, the median values of $\hat{q}$ become increasingly lower than expected, and the interquartile range increases. This is because it becomes progressively harder to evaluate the tail of the distribution (which has a major influence on the value of $\hat{q}$) as the number of points in the sample reduces. The median value of $\hat{\kappa}$ increases from the expected value as the number of points decreases, leading to an overestimate of the mean of the distribution. The median values of $\hat{q}$ and $\hat{\kappa}$ appear a reasonable match to the expected values q and κ down to $N \sim 100$, below which they are increasingly erroneous. Hence, this supports our previous decision to only present the MLE parameters for samples that have more than 100 points and we continue to use that limit in this study.

Figures 1c and 1d present the results of these simulations for two fixed sets of Weibull parameters typical of the PDFs observed in this paper; $c = 0.8$ and $\chi = 0.0015$ (red), and $c = 1.4$ and $\chi = 0.005$ (black). The layout of these panels is the same as described above for panels a and b. Similar to the q-exponential simulation, the MLE parameters become increasingly well defined as the number of points increases toward $N = 10{,}000$, with the median values matching those expected, and with increasingly smaller interquartile ranges. The MLE estimator $\hat{c}$ deviates from the expected value as the number of points decreases toward $N = 10$, whereas the median value of $\hat{\chi}$ stays close to the expected value of χ, although the interquartile range increases. Overall, the values of $\hat{c}$ and $\hat{\chi}$ are better estimated for lower numbers of data points than the q-exponential estimators. However, for consistency, we assume the same lower limit of $N = 100$ vorticity measurements in a sample as representing an adequate amount for an acceptable model fit.

2.4. Examples of PDF Component Separation and Model Fitting

Figure 2 presents examples of the PDF component separation analysis method described above. Figure 2a presents the analysis for the vorticity values measured between 0600 and 0700 MLT and 73° and 74° AACGM latitude, for the IMF B_y positive sub-group. The observed variations are typical of those seen in the auroral region, and are very similar to those presented in figure 5 of Chisham and Freeman (2023), although the uncertainty levels of the binned PDF values are greater here due to the lower number of vorticity measurements made in the smaller spatial area. The

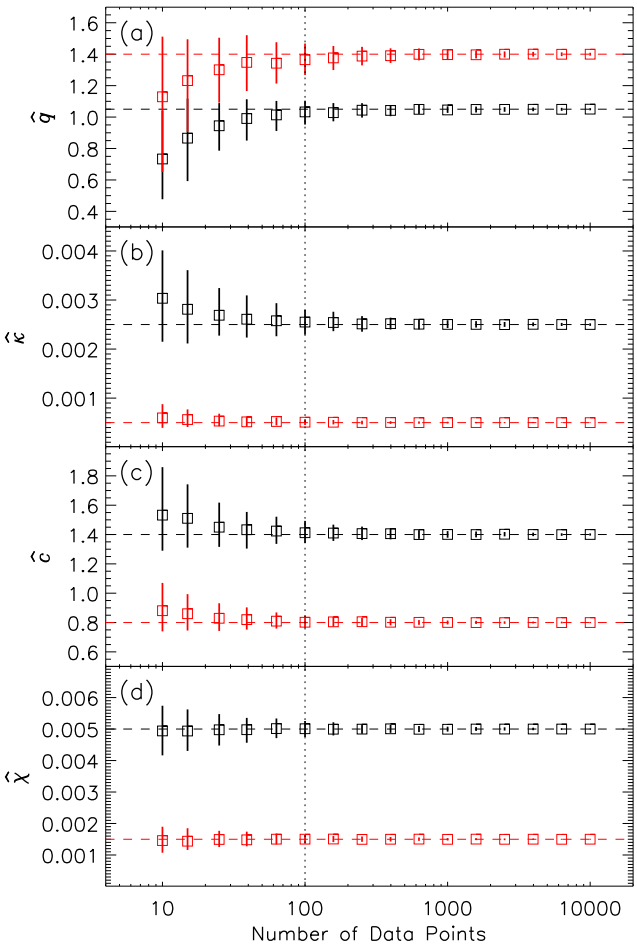

Figure 1. Results of a multiple Maximum Likelihood Estimation (MLE) analysis of simulated q-exponential and Weibull distributions of different sample sizes (given by the number of points on the *x*-axis). The square symbols represent the median values of the MLE estimators: (a) $\hat{q}$; (b) $\hat{\kappa}$; (c) $\hat{c}$; and (d) $\hat{\chi}$, from 1,000 different simulations of each sample size. The error bars represent the interquartile range of the results. In panels (a) and (b) the black symbols represent the results for simulated q-exponential distributions with $q = 1.05$ and $\kappa = 0.0025$ (highlighted by the black horizontal dashed lines); the red symbols represent the results for simulated q-exponential distributions with $q = 1.4$ and $\kappa = 0.0005$ (highlighted by the red horizontal dashed lines). In panels (c) and (d) the black symbols represent the results for simulated Weibull distributions with $c = 1.4$ and $\chi = 0.005$ (highlighted by the black horizontal dashed lines); the red symbols represent the results for simulated Weibull distributions with $c = 0.8$ and $\chi = 0.0015$ (highlighted by the red horizontal dashed lines).

black symbols and error bars represent the binned PDF values and uncertainties when considering all the vorticity values measured in this spatial region over the measurement epoch. In this example, the number of negative vorticity values measured (N_-) is greater than the number of positive vorticity values measured (N_+). Hence, the positive vorticity values are fit solely with a q-exponential distribution (solid black line), representing the MS component, assuming a complete absence of a LS component at this location with this sense of vorticity. In this case the MLE analysis for the positive vorticity values results in a q-exponential function with $\hat{q} = 1.17$, and $\hat{\kappa} = 0.0017$.

For the negative vorticity values, we use the method detailed above to statistically separate the measured vorticity values into two separate populations, representing the LS and MS components of the vorticity PDFs. In Figure 2a the blue symbols and error bars represent the binned PDF values and uncertainties of the negative MS vorticity values. These vorticity values are fit with a q-exponential distribution (solid blue line). In this case the MLE analysis results in a q-exponential function with $\hat{q} = 1.16$, and $\hat{\kappa} = 0.0018$, closely matching that for the positive vorticity values, as expected given the assumptions made in the methodology. In Figure 2a the red symbols and error bars represent the binned PDF values and uncertainties of the negative LS vorticity values. These vorticity values are fit with a Weibull distribution (solid red line), with the MLE analysis resulting in values of $\hat{c} = 1.62$ and $\hat{\chi} = 0.0045$. This analysis is repeated for every spatial location x_j, with the spatial variation of the resulting estimators presented in the following section.

In Figure 2b we present an example of this analysis for the vorticity values measured between 2000 and 2100 MLT and 68° and 69° AACGM latitude, which is typical of those seen in the sub-auroral region. The separation of distributions in this region was not considered by Chisham and Freeman (2023), and the major comments they made about the PDFs in this region were that they were very heavy-tailed, and that the distributions were approximately symmetric, although the mode of the distribution was shifted away from zero, the direction of the shift being dependent on whether the vorticity measurements were made in the dawn or dusk sector. Studying the typical large-scale convection in these regions suggests that there are no obvious shears or rotations in the large-scale flow that would result in a significant LS vorticity component. However, for consistency with the analysis of the PDFs measured in other spatial locations, we undertake the same separation analysis in these regions. The positive MS vorticity values have been fit by a q-exponential function with $\hat{q} = 1.50$ and $\hat{\kappa} = 0.0011$ (black line). The negative MS vorticity binned PDF values (blue symbols) are very similar to the total binned PDF values (black symbols) for this example. The negative MS vorticity values have been fit by a q-exponential function with $\hat{q} = 1.37$ and $\hat{\kappa} = 0.0012$ (blue line). The 'LS' component (red) is reduced in magnitude in comparison to the other example, and has been fit by a Weibull function with $\hat{c} = 0.93$ and $\hat{\chi} = 0.0013$. The shape of the 'LS' component is of a different form to that in Figure 2a, leading to a MLE Weibull fit with a value of $\hat{c} < 1.0$, rather than the more usual $\hat{c} > 1.0$. Weibull distributions with $c < 1.0$ tend to infinity as ω tends to zero, whereas Weibull distributions with $c > 1.0$ tend to zero as ω tends to zero. As a consequence of these differences, we cannot describe this 'additional' vorticity PDF component as a 'LS' component in the sub-auroral regions, and here we have labeled it as 'Unknown'. We will discuss the potential origins of this component later in the paper.

3. Results

In this section, we present the spatial variation of the MLE estimators for the LS and MS components of the vorticity PDFs for both IMF B_y positive and IMF B_y negative conditions separately.

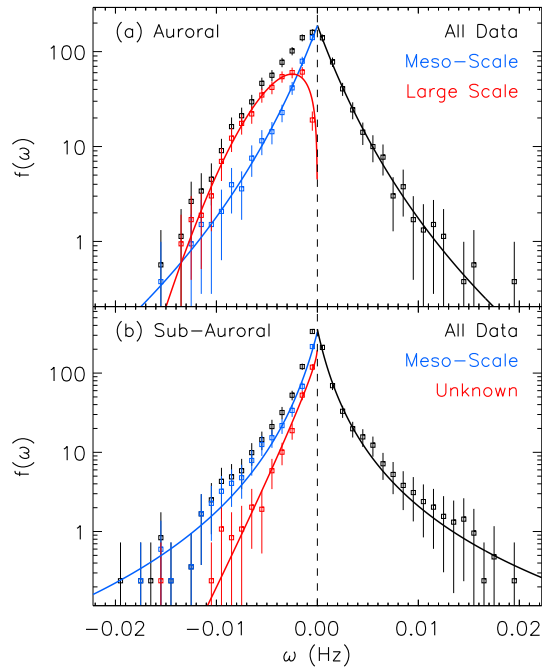

Figure 2. Example Probability Density Functions (PDFs) of vorticity measured in the high-latitude ionosphere and their Maximum Likelihood Estimation (MLE) fits. (a) Example PDF from the auroral region, covering the spatial bin between 0600 and 0700 MLT and 73° and 74° AACGM latitude. (b) Example PDF from the sub-auroral region, covering the spatial bin between 2000 and 2100 MLT and 68° and 69° AACGM latitude. The black square symbols represent the binned PDF values when considering all data, with the black error bars representing the uncertainty in these values. The black solid lines for positive vorticity values represent the q-exponential MLE fit to the positive vorticity data. The blue square symbols represent the binned PDF values for the meso-scale (MS) component, with the blue error bars representing the uncertainty in these values. The blue solid lines for negative vorticity values represent the q-exponential MLE fit to the negative MS vorticity data. The red square symbols represent the binned PDF values for the large-scale (LS) component (panel a), or the unknown component (panel b), with the red error bars representing the uncertainty in these values. The red solid lines represent the Weibull fits to the LS component data (panel a), or the unknown component data (panel b).

3.1. Large-Scale Vorticity

Figure 3 presents the spatial variation of the Weibull fit estimators ($\hat{c}$, $\hat{\chi}$) for the LS component during IMF B_y positive conditions. The left and right columns show the results for the positive vorticity and negative vorticity sides of the PDF, respectively. The LS component at any location can only exist for one sense of vorticity, and so the observational regions for the two senses of vorticity are mutually exclusive.

Figures 3a and 3b show the number of vorticity measurements contributing to the PDF at every location. The largest densities of LS vorticity measurements (∼200–2000 data points, colored green and yellow) are predominantly in the auroral zone, on the duskside for positive vorticity PDFs, and on the dawnside for negative vorticity PDFs; in these regions the MLE analysis is acceptable, or better. A similarly large density of measurements is found in the sub-auroral region, but with the opposite vorticity sense, with large values on the dawnside for positive vorticity PDFs, and on the duskside for negative vorticity PDFs. The smallest number of measurements are found within the polar cap and at low latitudes on the dayside (<∼100 data points). In these regions there are not enough data points for an accurate MLE of the fit parameters.

Figures 3c and 3d present the spatial variation of the $\hat{c}$ estimator. To aid the eye when interpreting the LS fit parameters, we have added equipotential contours of the statistical large-scale ionospheric plasma flow due to convection (red solid lines). These contours are taken from the climatological model of Thomas and Shepherd (2018) for neutral dipole tilt ($-10° \leq$ tilt $\leq 10°$) and moderate solar wind driving conditions ($1.6 \leq E_{SW} \leq 2.1$ mV/m, where E_{SW} is the solar wind electric field), and only contours with the same vorticity sense as the PDF fit parameters are shown, that is, contours of positive electrostatic potential for negative vorticity, and contours of negative electrostatic potential for positive vorticity. Figure 3c presents the variation of $\hat{c}$ for the locations for which the LS component is in the positive vorticity sense. Here, the 'melon'-shaped convection cell (red solid lines) in the duskside ionosphere has a positive vorticity. There is a LS vorticity component related to the vorticity of this cell; here, the value of $\hat{c}$ is quite variable, typically being between 0.9 and 1.3. The only other LS component for this sense of vorticity is located in the sub-auroral region on the dawnside. In this region, there is no large-scale convection flow with the same sense of vorticity, and as discussed above the use of the description 'LS' here is a misnomer, and hence, we label this component 'unknown'. Again, the value of $\hat{c}$ here is quite variable, typically being between 0.7 and 1.1. The potential source of this 'unknown' component is discussed later in the paper. Figure 3d presents the variation of $\hat{c}$ for the locations for which the LS component is in the negative vorticity sense. Here, the 'banana'-shaped convection cell (red solid lines) in the dawnside ionosphere has a negative vorticity. There is a LS vorticity component related to the vorticity of this cell; here, the value of $\hat{c}$ is quite consistent, being ∼1.2–1.4. Again, there is an additional 'unknown' component in the sub-auroral region, this time on the duskside, for which there is no associated large-scale convection flow with the same sense of vorticity. The value of $\hat{c}$ here is between ∼0.6 and 0.9.

Figures 3e and 3f present the spatial variation of the $\hat{\chi}$ estimator. Again, in these figures we show the equipotential contours of the large-scale convection flow. Figure 3e presents the variation of $\hat{\chi}$ for the locations for which the LS component is in the positive vorticity sense, the same as for the values of $\hat{c}$ in Figure 3c. Here, the value of $\hat{\chi}$ for the LS region on the duskside varies systematically from values of ∼0.005 at lower latitudes in the auroral zone to values of ∼0.001 in the polar cap. For the dawnside region that is unrelated to the large-scale convection flow, the value of $\hat{\chi}$ is ∼0.001–0.003. Figure 3f presents the variation of $\hat{\chi}$ for the locations for which the LS component is in the negative vorticity sense, the same as for the values of $\hat{c}$ in Figure 3d. Here, the value of $\hat{\chi}$ for

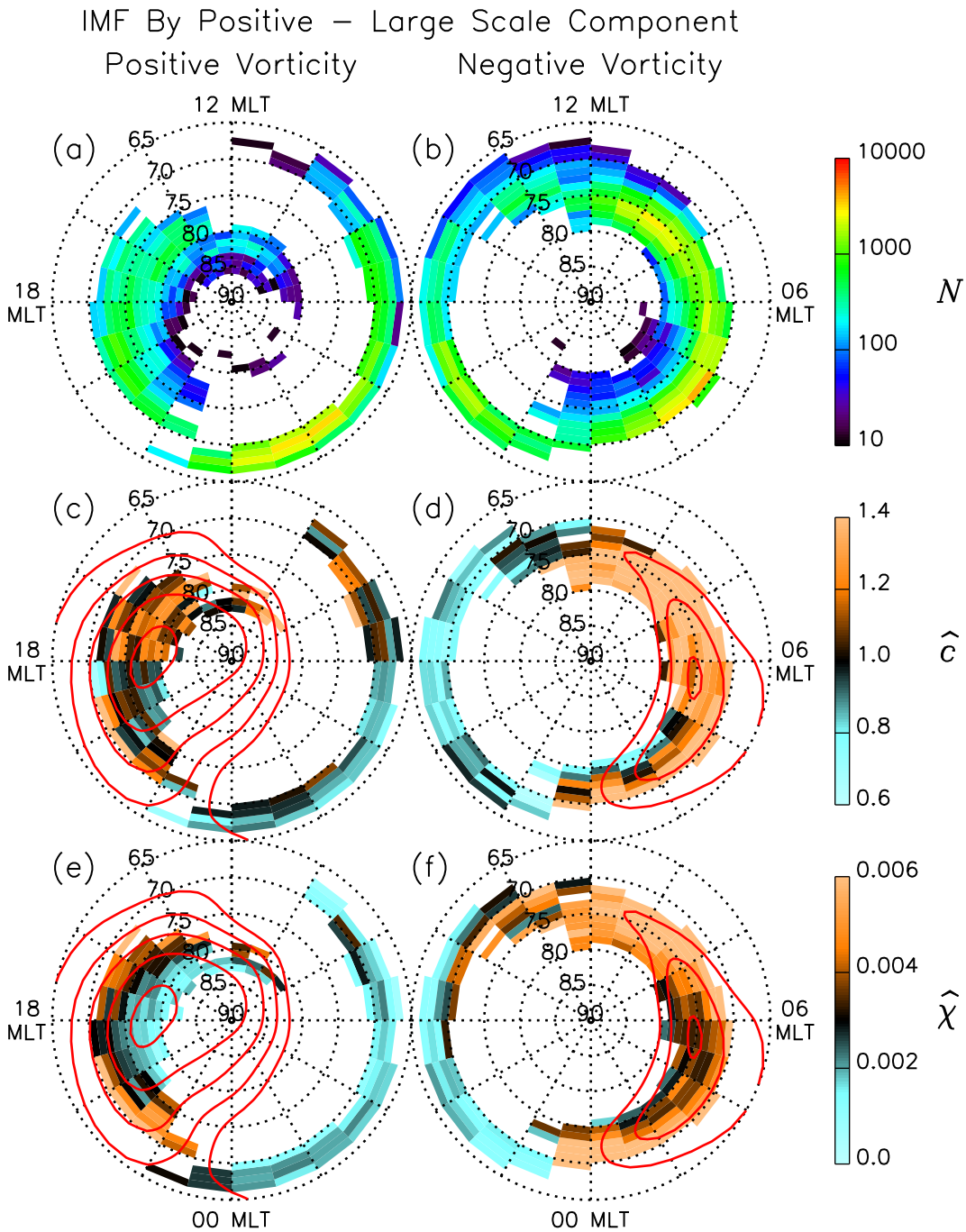

Figure 3. The spatial variation of the Weibull Maximum Likelihood Estimation (MLE) estimators $(\hat{c},\hat{\chi})$ for the large-scale (LS) component during IMF B_y positive conditions. Panels (a) and (b) present the occurrence values (N) of the number of vorticity measurements in each spatial bin, for positive vorticity and negative vorticity, respectively. Panels (c) and (d) present the values of $\hat{c}$ for each spatial bin, for positive and negative vorticity, respectively. Panels (e) and (f) present the values of $\hat{\chi}$ for each spatial bin, for positive and negative vorticity, respectively. The estimators $\hat{c}$ and $\hat{\chi}$ are only shown for bins for which $N \geq 100$. The red solid lines represent equipotentials of ionospheric convection for IMF B_y positive conditions, and for which the vorticity is in the same sense. These equipotentials are taken from the climatological model of Thomas and Shepherd (2018) for neutral dipole tilt ($-10° \leq$ tilt $\leq 10°$) and moderate solar wind driving conditions ($1.6 \leq E_{SW} < 2.1$ mV/m), and the contours are drawn at 6-kV intervals.

the LS region on the dawnside varies between ~0.003 and ~0.006, being lower before dawn. For the duskside region that is unrelated to the large-scale convection flow, the value of $\hat{\chi}$ is again ~0.001–0.003.

Figure 4 presents the spatial variation of the Weibull estimators ($\hat{c}$, $\hat{\chi}$) for the LS component during IMF B_y negative conditions. As with the LS estimators for IMF B_y positive presented in Figure 3, the LS component at any location can only exist for one sense of vorticity, and so the observational regions for the two senses of vorticity are mutually exclusive. The patterns observed in N (Figures 4a and 4b), $\hat{c}$ (Figures 4c and 4d), and $\hat{\chi}$ (Figures 4e and 4f), are very similar to the variations observed for IMF B_y positive in Figure 3, but mirrored around the noon-midnight meridian line, and for the opposite vorticity sense. This is to be expected as the large-scale convection during IMF B_y negative conditions is also an approximate mirror of that for IMF B_y positive conditions, as shown by the differences in the solid red equipotential contours between Figures 3 and 4.

Figures 4a and 4b show the number of vorticity measurements contributing to each LS PDF for IMF B_y negative conditions. The largest density of measurements are again in the auroral region, and again are on the duskside for the positive vorticity PDFs, and the dawnside for the negative vorticity PDFs, matching the expected vorticity of the convection cells in these regions. However, the size of the two regions has changed in contrast to the IMF B_y positive results with the extent of the duskside positive vorticity region being much greater than that of the dawnside negative vorticity region. Again, there is a large density of 'unknown' vorticity measurements in the sub-auroral region, again with large values on the dawnside for positive vorticity, and large values on the duskside for negative vorticity. The observed variations in the sub-auroral region are very similar to those observed for the IMF B_y positive case in Figure 3, suggesting that they are independent of the prevailing IMF direction.

Figures 4c and 4d show the variation of the $\hat{c}$ estimator for each LS vorticity PDF for IMF B_y negative conditions. Again, the red lines show the statistical equipotential contours of the large-scale flow from the model of Thomas and Shepherd (2018). In Figure 4c, the 'banana'-shaped convection cell on the duskside is associated with large values of $\hat{c}$ (>~ 1.2) on the dayside and at lower latitudes on the nightside, which transform into smaller values of $\hat{c}$ (~0.8 to 1.0) at higher latitudes on the nightside. Similar to the sub-auroral region results in Figure 3c, the value of $\hat{c}$ at lower latitudes on the dawnside varies between ~0.7 and 1.1. In Figure 4d, the 'melon'-shaped convection cell on the dawnside is associated with high values (~1.3) at lower latitudes, gradually decreasing to values ~0.9 to 1.1 at the edge of the polar cap. Similar to the sub-auroral region results in Figure 3d, the value of $\hat{c}$ at lower latitudes on the duskside varies between ~0.6 and 1.0.

Figures 4e and 4f show the variation of the $\hat{\chi}$ estimator for each LS vorticity PDF for IMF B_y negative conditions, with the accompanying equipotential contours. In Figure 4e, the 'banana'-shaped convection cell on the duskside is associated with large values of $\hat{\chi}$ (~0.004 to 0.006) at lower latitudes in the auroral zone, transforming to lower values (~0.001 to 0.003) in the polar cap. Similar to the sub-auroral region results in Figure 3e, the value of $\hat{\chi}$ at lower latitudes on the dawnside varies between ~0.001 and 0.003. In Figure 4f, the 'melon'-shaped convection cell on the dawnside is associated with high values (~0.005) at lower latitudes, gradually decreasing to values ~0.002 to 0.003 at the edge of the polar cap. Similar to the sub-auroral region results in Figure 3f, the value of $\hat{\chi}$ at lower latitudes on the duskside varies between ~0.0005 and 0.0025.

3.2. Meso-Scale Vorticity

Figure 5 presents the spatial variation of the q-exponential fit estimators ($\hat{q}$,$\hat{\kappa}$) for the MS component during IMF B_y positive conditions. Again, the left and right columns show the results for the positive vorticity and negative vorticity sides of the PDF, respectively. In contrast to the LS PDF results presented in Figures 3 and 4, the results for positive vorticity (panels a, c, and e) appear very similar to those for negative vorticity (panels b, d, and f); this is as expected owing to the assumption that the MS PDFs are symmetric in the methodology, and provides a check that the methodology is separating the vorticity populations as expected.

Figures 5a and 5b show the number of vorticity measurements contributing to the PDF at every location. The red regions highlight where there are the largest density of measurements (~10,000 data points); this number peaks in the auroral region in the nightside ionosphere. The darker blue regions highlight where there are the smallest density of measurements (<~100 data points); this number is small both at the highest latitudes, and at the lowest latitudes on the dayside. In these regions there are not enough data points for an accurate MLE of the fit parameters. The green regions (~200–2000 data points) dominate the rest of the high-latitude region.

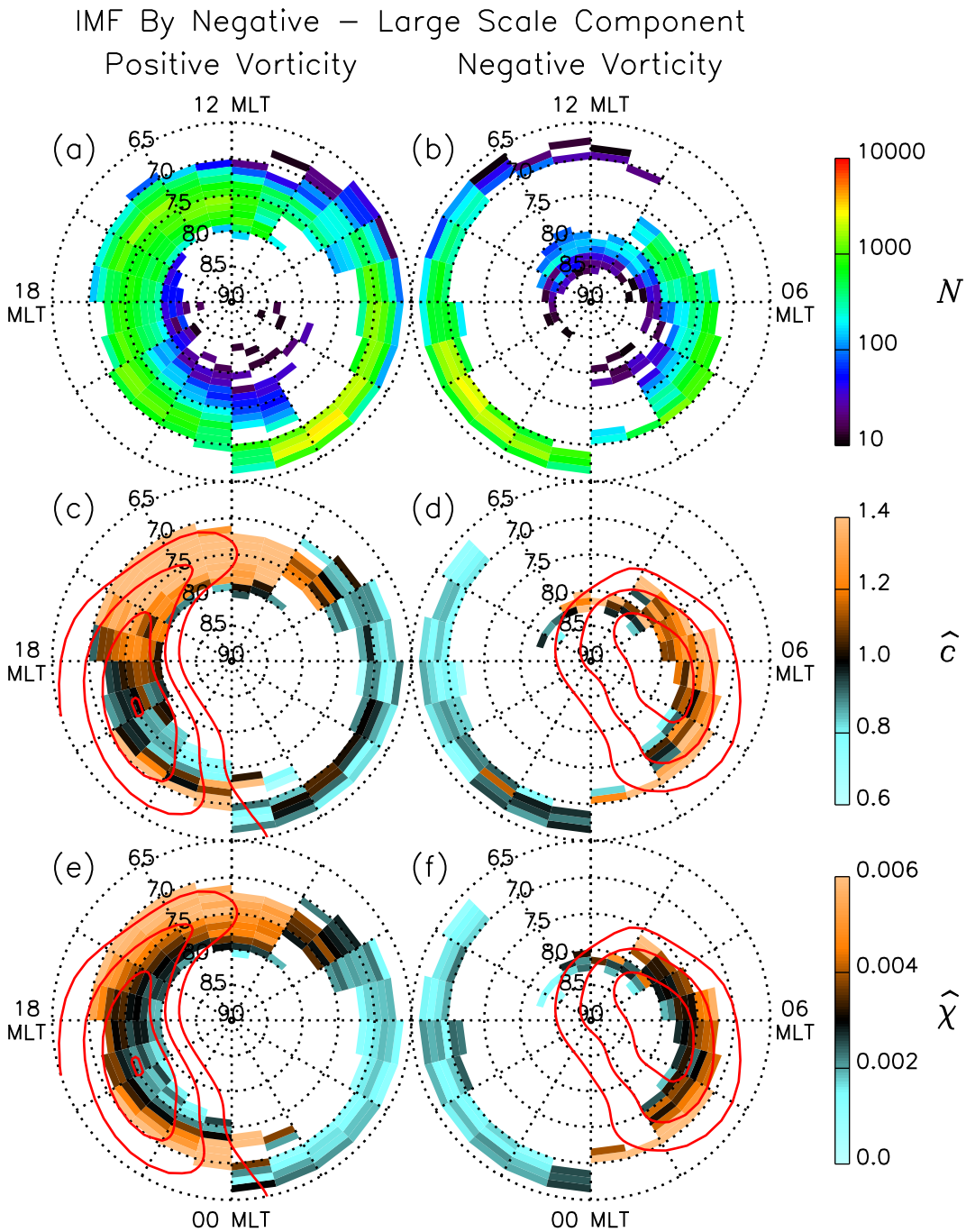

Figure 4. The spatial variation of the Weibull Maximum Likelihood Estimation (MLE) estimators $(\hat{c},\hat{\chi})$ for the large-scale (LS) component during IMF B_y negative conditions. Panels (a) and (b) present the occurrence values (N) of the number of vorticity measurements in each spatial bin, for positive vorticity and negative vorticity, respectively. Panels (c) and (d) present the values of $\hat{c}$ for each spatial bin, for positive and negative vorticity, respectively. Panels (e) and (f) present the values of $\hat{\chi}$ for each spatial bin, for positive and negative vorticity, respectively. The estimators $\hat{c}$ and $\hat{\chi}$ are only shown for bins for which $N \geq 100$. The red solid lines represent equipotentials of ionospheric convection for IMF B_y negative conditions, and for which the vorticity is in the same sense. These equipotentials are taken from the climatological model of Thomas and Shepherd (2018) for neutral dipole tilt ($-10° \leq$ tilt $\leq 10°$) and moderate solar wind driving conditions ($1.6 \leq E_{SW} < 2.1$ mV/m), and the contours are drawn at 6-kV intervals.

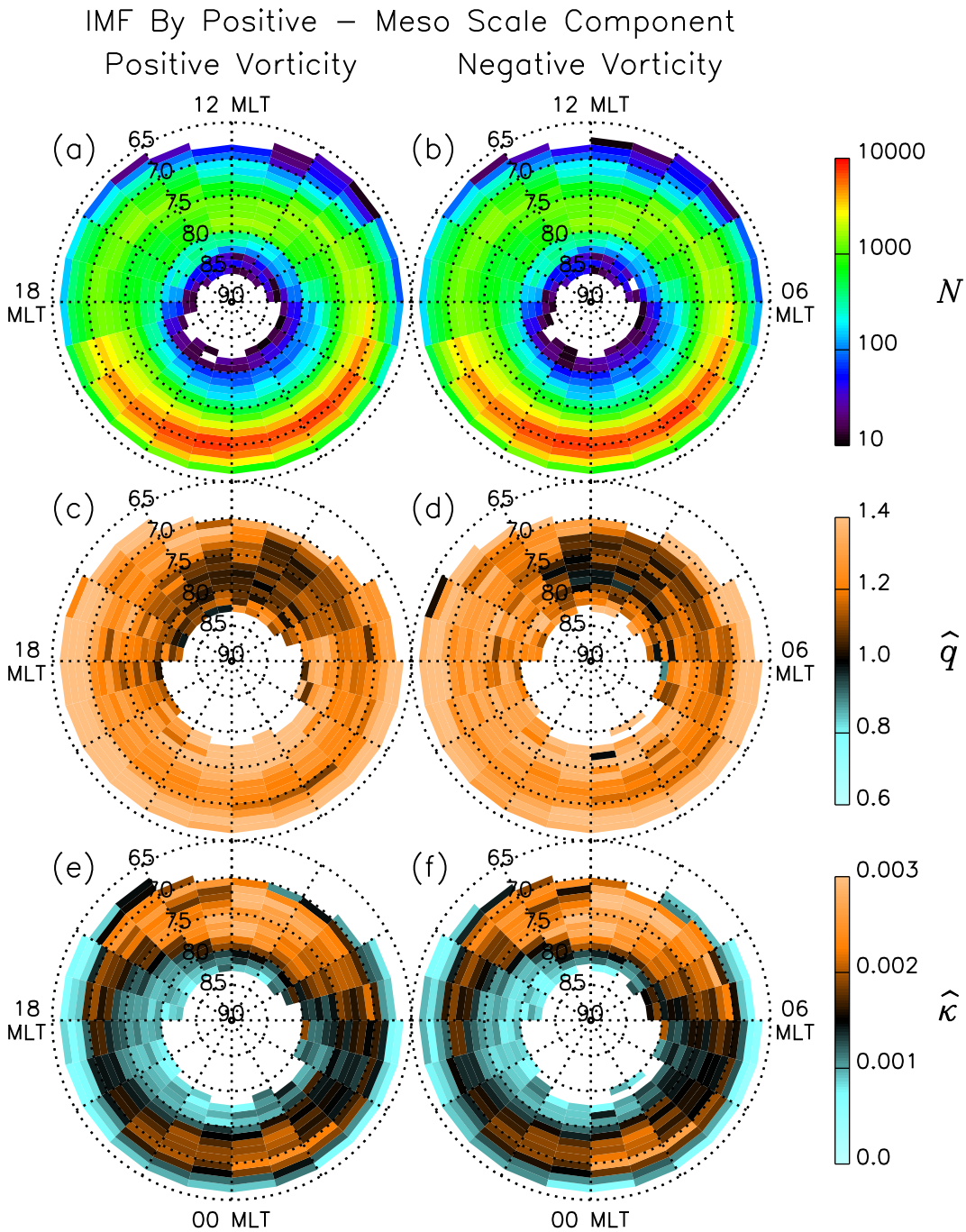

Figure 5. The spatial variation of the q-exponential Maximum Likelihood Estimation (MLE) estimators $(\hat{q},\hat{\kappa})$ for the meso-scale (MS) component during IMF B_y positive conditions. Panels (a) and (b) present the occurrence values (N) of the number of vorticity measurements in each spatial bin, for positive vorticity and negative vorticity, respectively. Panels (c) and (d) present the values of $\hat{q}$ for each spatial bin, for positive and negative vorticity, respectively. Panels (e) and (f) present the values of $\hat{\kappa}$ for each spatial bin, for positive and negative vorticity, respectively. The estimators $\hat{q}$ and $\hat{\kappa}$ are only shown for bins for which $N \geq 100$.

Figures 5c and 5d present the spatial variation of the $\hat{q}$ estimator. First, it is clear that the estimated value of $\hat{q}$ rarely (almost never) dips below 1.0; this means that the MS PDFs are always heavier-tailed than an exponential (for which $q = 1$). However, there is a large region, shifted slightly dawnside of noon, where the value of $\hat{q}$ is consistently in the range 1.0–1.1; this location matches the ionospheric projection of the magnetospheric cusp

region where small-scale turbulent flow is prevalent (Di Mare et al., 2021). Around the rest of the auroral oval the value of $\hat{q}$ is larger, being ∼1.2 to 1.3. The largest values of $\hat{q}$ (often >1.4), are found in the sub-auroral region and the nightside polar cap. This matches the more leptokurtic PDFs typically seen there, such as that in the example presented in Figure 2b.

Figures 5e and 5f present the spatial variation of the $\hat{\kappa}$ estimator. The largest values of $\hat{\kappa}$ (>∼ 0.002) are found in the dayside auroral oval and polar cap, including the cusp region; this indicates that the widest vorticity PDFs are found in this region. Much of the auroral region at other MLTs is also characterized by relatively large values of $\hat{\kappa}$ (>∼ 0.0015). The lowest values of $\hat{\kappa}$ (<∼ 0.001) are found in the sub-auroral region and the polar cap; these regions are characterized by the thinnest vorticity PDFs.

Figure 6 presents the spatial variation of the q-exponential fit estimators ($\hat{q}$, $\hat{\kappa}$) for the MS component during IMF B_y negative conditions. As with the previous figures, the left and right columns show the results for positive vorticity and negative vorticity measurements, respectively. Again, as with the IMF B_y positive MS vorticity results (Figure 5), the results for positive vorticity (panels a, c, and e) appear very similar to those for negative vorticity (panels b, d, and f), as expected. Not only this, they appear very similar to the MS results for IMF B_y positive, as presented in Figure 5. The spatial variation of vorticity occurrence numbers (Figures 6a and 6b) again show the largest density of values in the nightside auroral region (∼10,000), and the smallest density of values at low latitudes on the dayside, and within the nightside polar cap (∼10 to 100). The spatial variation of the $\hat{q}$ estimator (Figures 6c and 6d) is again lowest in the cusp region (∼1.0 to 1.1), increasing slightly within the auroral region (∼1.2 to 1.3), and largest in the sub-auroral region and the nightside polar cap (>∼1.4). The spatial variation of the $\hat{\kappa}$ estimator (Figures 6e and 6f) is again largest in the dayside auroral oval, polar cap, and cusp (>∼0.002), slightly lower in the rest of the auroral region (>∼0.0015), and lowest in the sub-auroral region and the nightside polar cap (<∼0.001).

As discussed in relation to Figure 5, the similarities between the positive and negative vorticity results were expected, due to the assumptions made in the methodology. However, the similarities between the results for positive and negative IMF B_y are not due to the methodology and suggest that the spatial variation of the MS vorticity component is independent of the prevailing IMF direction. Consequently, the sources of the meso-scale plasma flow vorticity may be dominated by processes unrelated to the direction of the prevailing IMF.

4. Discussion

Here, we present a summary of the typical LS and MS vorticity PDFs that we have observed in different regions of the ionosphere, and discuss the potential origins of the vorticity in each of these regions. We also discuss the consequences of not including the velocity variations associated with meso-scale vorticity in ionospheric plasma flow models, and how this component might be added to existing or future models.

4.1. Large-Scale Vorticity

We start by considering the better-understood sources of LS vorticity. Figure 7 presents representations of the typical LS Weibull vorticity PDFs observed in different regions of the ionosphere. These are all one-sided distributions, and are presented for the case of negative large-scale vorticity. Similar (but reflected) distributions exist for the case of positive large-scale vorticity in other regions of the ionosphere.

Figure 7a presents the typical LS Weibull vorticity distributions that are observed in the 'banana' convection cells for the auroral (black) and polar cap (red) regions. The auroral Weibull is defined here by $c = 1.4$ and $\chi = 0.005$, whereas the polar cap Weibull is defined here by $c = 1.4$ and $\chi = 0.002$. The vertical dotted lines highlight the median vorticity for each of these distributions. Although the shape of these Weibull distributions is the same, the scale is significantly different, with much larger values typically observed within the auroral region. This is clear from the increased width of the distribution as well as the larger median. To give some context for the observed vorticity values, if the auroral region median value is assumed to be purely the result of a flow shear across the measurement cell, then this median flow shear Δv ranges from ∼400 to ∼800 m/s, depending on the measurement cell size.

Figure 7b presents the typical LS Weibull vorticity distributions that are observed in the 'melon' convection cells for the auroral (black) and polar cap (red) regions. Here, the auroral Weibull is defined by $c = 1.1$ and $\chi = 0.004$, whereas the polar cap Weibull is defined by $c = 1.1$ and $\chi = 0.002$. The value of c is much lower than that seen in the

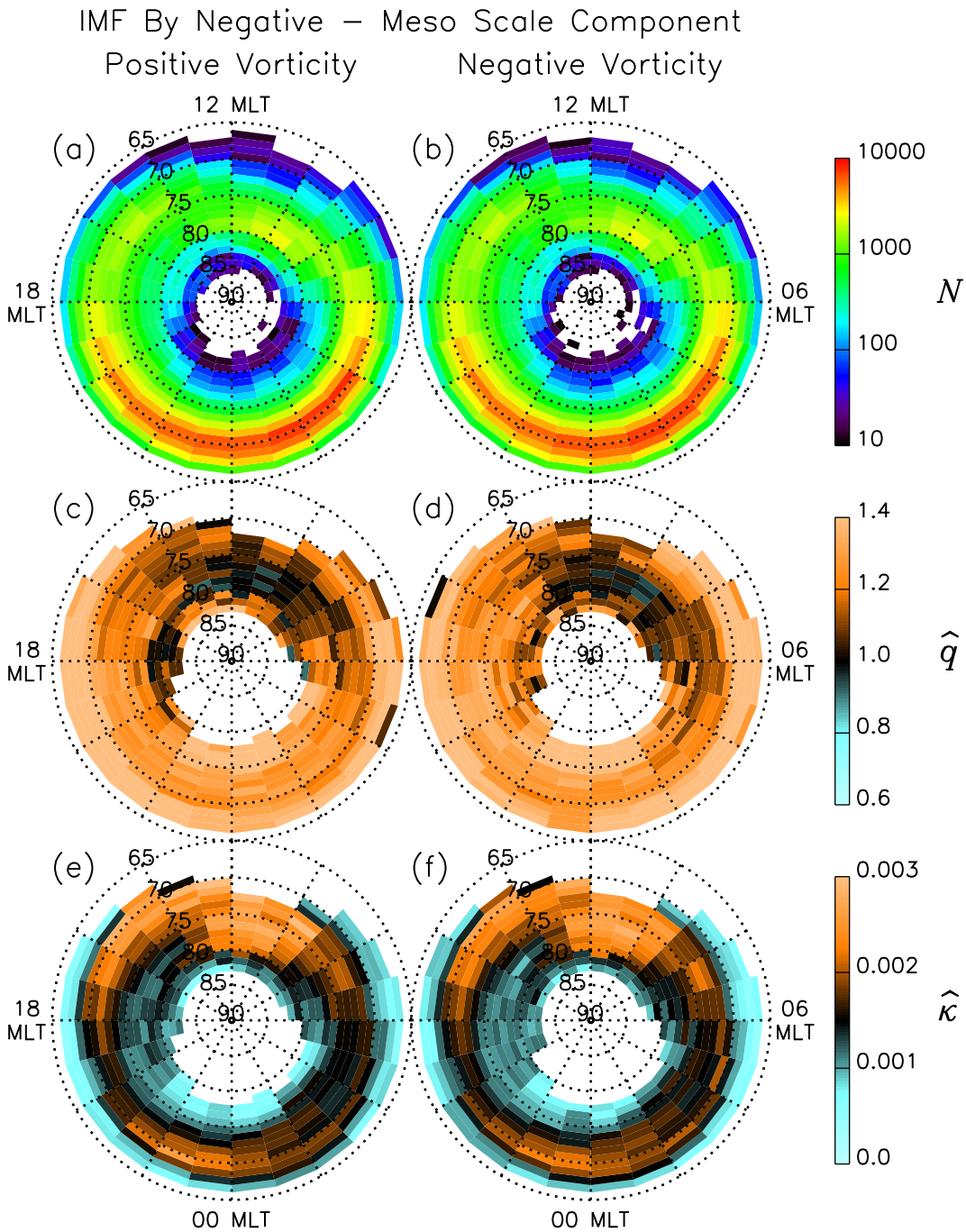

Figure 6. The spatial variation of the q-exponential Maximum Likelihood Estimation (MLE) estimators $(\hat{q},\hat{\kappa})$ for the meso-scale (MS) component during IMF B_y negative conditions. Panels (a) and (b) present the occurrence values (N) of the number of vorticity measurements in each spatial bin, for positive vorticity and negative vorticity, respectively. Panels (c) and (d) present the values of $\hat{q}$ for each spatial bin, for positive and negative vorticity, respectively. Panels (e) and (f) present the values of $\hat{\kappa}$ for each spatial bin, for positive and negative vorticity, respectively. The estimators $\hat{q}$ and $\hat{\kappa}$ are only shown for bins for which $N \geq 100$.

'banana' cell, and is approaching unity, at which point the distribution would be exponential. Even though these distributions are heavier-tailed than those seen in Figure 7a, the median value, and hence, the typically observed value is lower than those seen in the 'banana' cell. This is as would be expected as the 'banana' cell is typically characterized by larger flow shears than the 'melon' cell. Again, for context, assuming that this auroral region

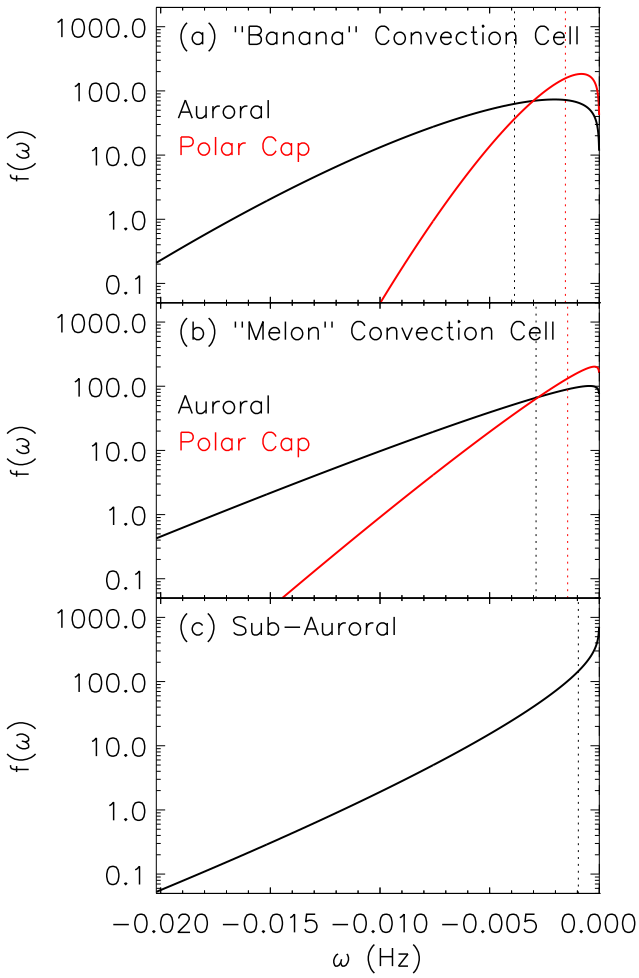

Figure 7. Examples of typical Weibull-distribution 'Large-scale' (LS) Probability Density Functions (PDFs) observed in the polar ionosphere. (a) Typical Weibull distributions observed in the 'Banana' convection cell. The black line is typical of the auroral region ($c = 1.4, \chi = 0.005$); the red line is typical of the polar cap ($c = 1.4, \chi = 0.002$). (b) Typical Weibull distributions observed in the 'Melon' convection cell. The black line is typical of the auroral region ($c = 1.1, \chi = 0.004$); the red line is typical of the polar cap ($c = 1.1, \chi = 0.002$). (c) Typical Weibull distribution observed in the sub-auroral region ($c = 0.8, \chi = 0.0015$). The vertical dotted lines in each panel represent the median values of each distribution.

median vorticity is purely the result of a flow shear, then Δv ranges from ~300 to ~600 m/s, again depending on the measurement cell size.

To help place the typical vorticity observations into further context, in Figure 8 we present a basic schematic representation of the different vorticity components in the polar ionosphere. The different ionospheric regions are approximately identified; the cusp (dark-gray shading), the auroral region (light-gray shading), and the polar cap and sub-auroral region (white). The blue lines and vortices in Figure 8 represent the LS sources of vorticity. The contours present example equipotentials from the model of Thomas and Shepherd (2018) for IMF B_y positive conditions.

The model contours represent a statistical average of the actual flow during these conditions, and so the vorticity apparent in the equipotential flow contours represents a highly smoothed version of reality. The PDFs presented in Figures 7a and 7b clearly show that the typical LS flow vorticity in the auroral region is much higher than that seen in the polar cap. The model contours are suggestive that this is the case, with the largest flow shears being located toward the poleward edge of the auroral oval, near the polar cap boundary. Indeed, Heppner and Maynard (1987) combined spacecraft data in an adaptive co-ordinate system (Chisham, 2017) to develop empirical models of the large-scale flow. These clearly show regions of much larger vorticity in the auroral region compared to the polar cap. This difference is not as immediately obvious in most empirical models which usually use non-adaptive geomagnetic co-ordinate systems, which tend to spatially smooth such features.

Figure 7c presents the typical 'unknown' Weibull distribution that is observed in the sub-auroral region. This sub-auroral Weibull is defined by $c = 0.8$ and $\chi = 0.0015$. The sense of this additional vorticity component is opposite to that of the convection cell in that sector, for example, the additional vorticity is positive on the dawnside in contrast to the negative vorticity convection cell observed there. In Figure 8, this component is represented by the small blue vortices. This vorticity is clearly not related to any large-scale variations in the convection flow (blue contours in Figure 8) and is likely to represent an additional single-sided meso-scale component on top of the symmetric MS vorticity PDFs that are also observed. Hence, our assumption of a symmetric MS distribution may not hold in the sub-auroral region. We discuss the potential origin of this component with those of the MS components below.

4.2. Meso-Scale Vorticity

Figure 9 presents representations of the typical MS q-exponential vorticity PDFs observed in different regions of the ionosphere. These are all symmetric two-sided distributions, following the assumptions made earlier in the paper. The four panels of the figure represent typical distributions observed in (a) the cusp region, (b) the auroral region, (c) the polar cap, and (d) the sub-auroral region. It is also important to remember that a contribution to these distributions comes from measurement and algorithmic errors and uncertainties (Chisham & Freeman, 2023).

The cusp q-exponential PDF (Figure 9a) is defined here by $q = 1.05$ and $\kappa = 0.0025$. In this region, meso-scale vortices are predominantly directly driven by solar wind and IMF fluctuations in the form of the ionospheric signature of FTEs (Provan et al., 1998), RFEs (Rinne et al., 2007), or TCVs (Friis-Christensen et al., 1988). Given the large value of the scale parameter κ for the MS vorticity PDF in the cusp, the MS vorticities observed there are typically large compared to other regions, suggesting strong turbulent flow driven by solar wind-magnetosphere interactions. This is depicted by the thick red vortices in the schematic diagram in Figure 8, with the increased thickness of the vortices representing an increase in the typical vorticity magnitudes. The vorticity PDFs observed in the cusp are almost exponential in character due to the low value of the shape parameter q. This parameter is a measure of intermittency, which describes the likelihood of the occurrence of extreme values compared to what

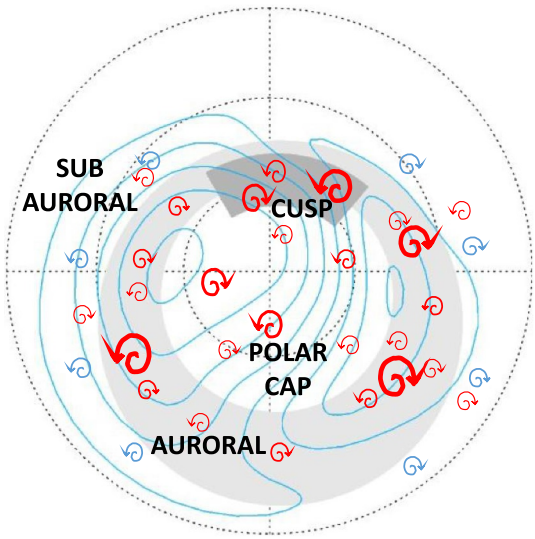

Figure 8. Schematic visualization of large-scale and meso-scale vorticity in the polar ionosphere. The white region at low latitudes represents the sub-auroral region. The light gray region represents the auroral region. The dark gray region represents the cusp region. The white region at high latitudes represents the polar cap. The blue contours represent typical equipotential flow contours for IMF B_y positive conditions. The blue vortices are a schematic representation of the 'large-scale' vorticity component observed in the sub-auroral region. The red vortices are a schematic representation of the meso-scale vorticity component seen in all regions. The thickness of the vortices helps to visualize the different vorticity magnitudes typically observed in different spatial regions.

would be expected from a normal distribution of values (Frisch, 2010). The low q values, and less leptokurtic distributions, typically observed in the cusp suggest a low level of intermittency. These observations are in contrast to those of Abel et al. (2009) who suggested that intermittency in the cusp plasma flow was inherited from the solar wind through solar wind-magnetosphere-ionosphere coupling processes, such as magnetic reconnection. Given this low intermittency, the likelihood of very extreme values of MS vorticity is much lower in the cusp than in other regions of the ionosphere.

The auroral region q-exponential PDF (Figure 9b) is defined here by $q = 1.3$ and $\kappa = 0.002$. Meso-scale phenomena here are driven by turbulent plasma flows in regions of large flow shear (Basu et al., 1988), and by features such as auroral arcs (Moen et al., 2008) and omega bands (Wild et al., 2000), which are driven indirectly by magnetotail processes. The more leptokurtic PDFs observed here imply that MS vortical flows in the auroral region are more intermittent than in the cusp. Combined with the wider nature of the observed PDFs, the likelihood of extreme MS vorticity in this region is larger than any other region in the high-latitude ionosphere, as portrayed by the thicker red vortices in the schematic diagram in Figure 8. To place the cusp and auroral region vorticity values into context, if we assume that the vorticity is due wholly to a vortical flow around the measurement cell, then a typical value of $\omega = 0.005$ Hz relates to a vortical flow speed of $v \sim 125$–250 m/s, depending on the measurement cell size.

Comprehensively characterizing the MS vorticity in the polar cap and the sub-auroral region is more challenging with the present data set as the SuperDARN vorticity measurements only partially cover these regions. There is a large hole surrounding the AACGM pole where we have no vorticity measurements. Similarly, at lower latitudes the measurements only extend partially into the sub-auroral region. Consequently, the MS vorticity measured in these regions should only be viewed as provisional and only a limited interpretation is possible. Since the vorticity measurements made in this paper were made (in the years 2000–2005 inclusive), the SuperDARN network coverage has expanded significantly, and now enables the measurement of plasma flows in both these regions (Nishitani et al., 2019). Hence, future work will expand the vorticity analysis into these regions.

The polar cap region q-exponential PDF (Figure 9c) is defined here by $q \sim 1.4$, $\kappa \sim 0.001$. This represents vorticity observations most likely poleward of, but close to, the polar cap boundary on the nightside, and in the dawn and dusk regions. It is possible that MS phenomena observed here are remnants of solar-wind driven vortical flows that have advected from the cusp region amongst the large-scale convection flow. Field-aligned current systems associated with dayside reconnection events such as flux transfer events have been shown to advect into the polar cap in this way (Milan et al., 2000; Nishimura et al., 2014; Sandholt et al., 1990), carrying MS vortical flow regions with them. Comparing this typical polar cap PDF with that from the cusp region shows that the vorticity values are much smaller, indicating that these current systems and the associated vortical flows will have weakened while advecting into the polar cap, as represented by the relatively thinner red vortices in Figure 8. However, the PDFs here are much more leptokurtic suggesting that the flow has become more intermittent as it moves from the cusp into the polar cap. As these measurements are generally made close to the polar cap boundary, it may be that this intermittency has been introduced by the motion of the boundary backward and forward across the measurement location, in response to changing levels of magnetic reconnection. Future expansion of the observation region, as discussed above, or analysis of the vorticity in an adaptive co-ordinate system (Chisham, 2017), should clarify this uncertainty.

The sub-auroral region q-exponential PDF (Figure 9d) is defined here by $q \sim 1.4$, $\kappa \sim 0.0005$. The meso-scale vortical flows in this region will be partially inherited from the nightside auroral zone, including those associated with substorm processes. Other potential sources of vorticity in this region include: (a) Fragmented and filamentary region 2 field-aligned currents originating in the ring current, as discussed in Chisham and

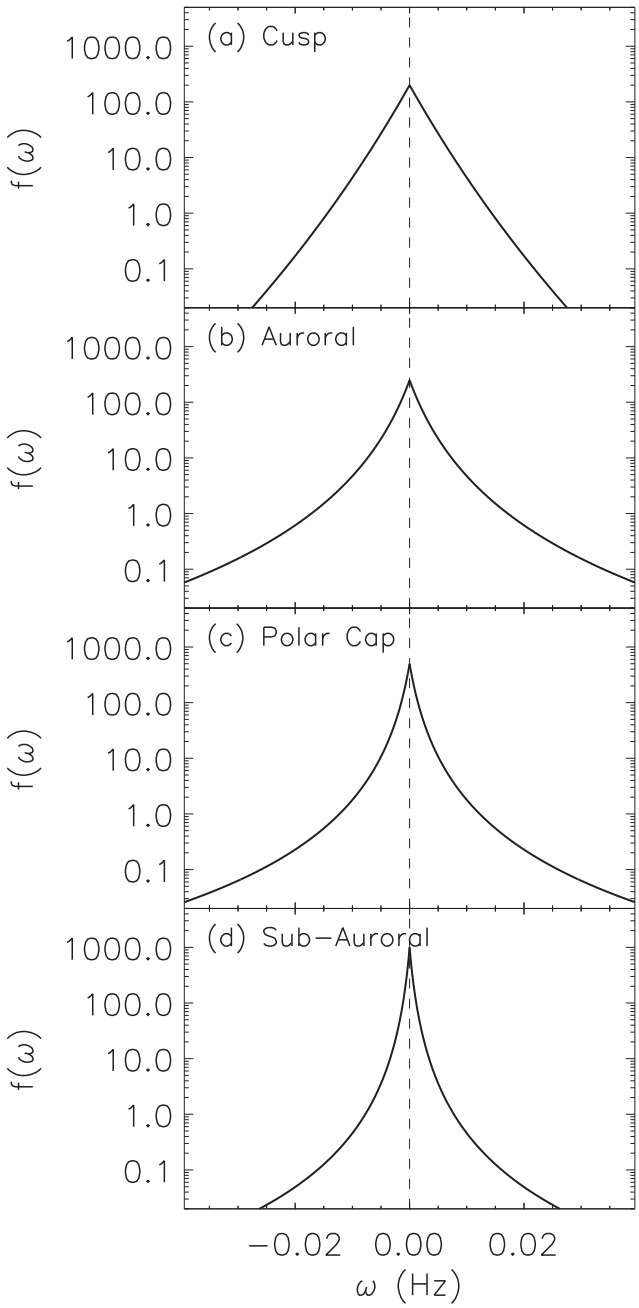

Figure 9. Examples of typical q-exponential-distribution 'Meso-scale' (MS) Probability Density Functions (PDFs) observed in the polar ionosphere. (a) Typical q-exponential distribution observed in the cusp region ($q = 1.05$, $\kappa = 0.0025$). (b) Typical q-exponential distribution observed in the auroral region ($q = 1.3$, $\kappa = 0.002$). (c) Typical q-exponential distribution observed in the polar cap ($q = 1.4$, $\kappa = 0.001$). (d) Typical q-exponential distribution observed in the sub-auroral region ($q = 1.4$, $\kappa = 0.0005$).

Freeman (2021, 2023); (b) TCVs driven by solar wind pressure fluctuations on the dayside of the Earth (Moretto & Yahnin, 1998); and (c) flow shears or gradients associated with fast sub-auroral flows such as Sub-Auroral Polarization Streams (SAPS) (Clausen et al., 2012; Sangha et al., 2020). The much thinner PDFs observed in this region imply that MS vorticity measurements will typically be much lower in these regions (as shown in Figure 8), even though a similar value of q to that seen in the polar cap suggests a high level of intermittency and hence, an increased probability of extreme vorticity measurements.

The sub-auroral region also contains the small 'unknown' vorticity population with the single-sided PDF presented in Figure 7c. This population is most likely due to the fragmented and filamentary region 2 field-aligned currents, which are predominantly downward in the dusk sector (leading to isolated anti-clockwise flow vortices), and predominantly upward in the dawn sector (leading to isolated clockwise flow vortices). To place this additional sub-auroral vorticity component into context, if we assume that the vorticity is due wholly to a vortical flow around the measurement cell, then the median vorticity value shown in Figure 7c relates to a vortical flow speed of $v \sim 25$ m/s for the measurement cell sizes in the sub-auroral region.

The fact that we observe the same spatial variation in meso-scale vorticity characteristics for different IMF directions suggests that flow fluctuations on these scales are dominantly driven by processes within the magnetosphere and ionosphere, such as turbulence, rather than being directly driven by changes in the IMF. The IMF is known to exert a significant control on the large-scale convection flow pattern, but its impact on the meso-scale flow is unclear. The IMF data in this study have been lagged to the Earth's bow shock. The impact of these IMF changes on the dayside ionospheric flows is expected to be relatively fast. However, there is an increased delay to any impact on the nightside and sub-auroral flows. This could provide another explanation for why the meso-scale flows in these regions appear invariant with changes in the IMF B_y direction. Although this would not explain why they appear invariant in the cusp and polar cap regions.

There are also other factors that may be controlling the meso-scale flow that we have not considered. As discussed in Chisham and Freeman (2023), large vorticity on the nightside may be associated with short substorm intervals of strong flows, which are interspersed with longer, quieter intervals. These flows would not be directly ordered by the IMF direction. Future work needs to consider organizing the ionospheric vorticity distributions on the nightside by their relation to substorm occurrence. In addition, separating the data set by season will help to determine if changing levels of ionospheric conductance have a role in controlling the different characteristics observed in the dayside and nightside ionosphere.

4.3. Consequences for Ionospheric Plasma Flow Models

As discussed in the Introduction, there are a large number of empirical models of ionospheric plasma flow (and associated electric field) that have been derived from both spacecraft and ground-based measurements. As a result of the methods used in the development of these models, they typically average out fluctuations below the large-scale. Similarly, in physics-based models of ionospheric plasma flow, often only the large-scale processes are captured. Hence, these models do not accurately represent the fluctuations in the flow on both the meso-scale and the small scale. For many applications, this simplification is acceptable. However, for accurate estimation of Joule

heating, and the electron density structure of polar cap patches, the effects of meso-scale fluctuations are often significant.

In order for operational models of ionsopheric plasma flow to improve, they need to start to consider fluctuations on both the meso-scale and the small scale. The big question is how this can be achieved in a practical way. This paper has provided a first attempt at assessing the potential contribution of meso-scale fluctuations to the flow, in terms of the vorticity associated with these fluctuations. However, how these vorticity fluctuations can be introduced into plasma flow models needs to be a major area of future study.

There are many statistical aspects of vorticity that need to be understood before such fluctuations can be confidently added to models. One important aspect is how persistent in time flow vorticity is in different locations? That is, are the vorticity measurements at a particular location random from one measurement to the next, or does their sense and magnitude persist? The more random variations are likely to exist in regions where there is a limited large-scale component and the meso-scale component is dominated by intermittent fluctuations. Hence, these fluctuations may be more easily modeled in a probabilistic sense, using model distributions of vorticity like those presented here. If the vorticity measured at a location is persistent, then there is a need to understand the reason for this persistence to be able to model it. This may be particularly true of regions dominated by the large-scale flow or of meso-scale fluctuations in the cusp region which appear to be directly driven by interactions with the solar wind, with low intermittency. Hence, there is a need to study the temporal variation of vorticity at different locations and over different time scales.

If meso-scale vorticity fluctuations in the cusp are deterministic (and as a consequence, possibly in the polar cap as well), then it is important to have a model for their occurrence following changes in the solar wind, whether that is large changes in solar wind pressure, or the presence of FTEs following southward turnings of the IMF. One way of achieving this would be to undertake a superposed epoch analysis of the meso-scale vorticity PDFs at different locations relative to large changes in solar wind pressure. Similarly, the effect of FTEs could be studied initially by a superposed epoch analysis relative to southward turnings in the IMF. Similar studies may be needed in the auroral region in response to substorms or other nightside reconnection events.

In regions of the ionosphere where the meso-scale vorticity fluctuations are more intermittent, a study of the temporal variation of vorticity may provide an answer as to whether it is suitable to represent the vorticity in these regions in a probabilistic way. This may be particularly relevant to the vorticity that is observed in the sub-auroral and polar cap regions.

Small-scale fluctuations in the ionospheric flow (on scales $< \sim$1–10 km) are difficult to measure in a continuous and systematic way, being below the spatial resolution of most techniques and instrumentation used to measure ionospheric plasma flow, such as SuperDARN. Understanding and modeling fluctuations on these scales will require a different approach, as it is not presently possible to measure vorticity on these scales, although the presence of small-scale ionospheric turbulence and intermittency has been identified and measured (Spicher et al., 2015, 2022). SuperDARN measurements of Doppler spectral width can provide an indirect measure of the level of sub-grid-scale structure and turbulence (Spicher et al., 2022; Vallières et al., 2004). It may be possible to use these measurements to provide a probabilistic parameterization of the sub-grid small-scale fluctuations in the flow for modeling purposes. This would require a better understanding of the factors that influence the measured spectral width, which include the small-scale spatiotemporal structure of irregularities in a grid cell, small-scale turbulence, and time-varying electric field variations due to both wave activity and gradients in the large and meso-scale structure (André et al., 2000; Villain et al., 2002).

5. Summary and Conclusions

In this paper we have used a method to statistically separate PDFs of vorticity into components related to the large and meso-scale components of the ionospheric flow. The large-scale vorticity appears to be driven wholly by the large-scale convection flow resulting from magnetic reconnection, and is well-represented in ionospheric flow models. This component varies with changes in the prevailing IMF as expected. The spatial variation of meso-scale vorticity appears to be independent of the prevailing IMF, suggesting that it is driven by transient solar wind phenomena and internal magnetospheric processes, such as turbulence. However, the character of the meso-scale vorticity component does vary systematically with location in the ionosphere.

1. In the cusp, the meso-scale vorticity is strongest and most likely driven by transient phenomena associated with the coupling of the solar wind and IMF with the magnetosphere.
2. In the polar cap, the meso-scale vorticity may be driven by remnants of the meso-scale cusp structure that are advecting with the large-scale flow, but decreasing in strength with increased intermittency.
3. In the auroral region, the meso-scale vorticity is strong and is most likely to be driven by nightside processes such as substorms, and by increased turbulent flows associated with flow shears.
4. In the sub-auroral region, the meso-scale vorticity is smallest, but the most intermittent. It is likely to be driven by fragmented and filamentary region 2 field-aligned currents.

In order to be able to adequately represent these meso-scale fluctuations in ionospheric flow models, we need to be able to fully understand the sources of these flow components, and how they vary in time in different locations.

Data Availability Statement

The SuperDARN vorticity data used in this paper are available through Chisham (2023), https://doi.org/10.5285/8EEDC594-730B-4AAD-B9CE-827912320C3A. The raw SuperDARN data are available through the BAS SuperDARN data mirror (https://www.bas.ac.uk/project/superdarn/).

Acknowledgments
GC and MPF were supported by the UK Natural Environment Research Council (NERC) highlight topic grant NE/W003066/1 (FINESSE). They were also funded as part of the British Antarctic Survey (BAS) Polar Science for a Sustainable Planet Programme, funded by NERC. The authors acknowledge the use of SuperDARN data. SuperDARN is a collection of radars funded by the national scientific funding agencies of Australia, Canada, China, France, Italy, Japan, Norway, South Africa, UK, and United States. The authors would like to thank the SuperDARN PIs of the radars which provided the original data for the vorticity data products: Kathryn McWilliams (University of Saskatchewan, Canada); J. Michael Ruohoniemi (Virginia Tech, USA); William Bristow (Penn State University, USA).

References

Abel, G. A., Freeman, M. P., & Chisham, G. (2006). Spatial structure of ionospheric convection velocities in regions of open and closed magnetic field topology. *Geophysical Research Letters*, *33*(24), L24103. https://doi.org/10.1029/2006GL027919

Abel, G. A., Freeman, M. P., & Chisham, G. (2009). IMF clock angle control of multifractality in ionospheric velocity fluctuations. *Geophysical Research Letters*, *36*(19), L19102. https://doi.org/10.1029/2009GL040336

Abel, G. A., Freeman, M. P., Chisham, G., & Watkins, N. W. (2007). Investigating turbulent structure of ionospheric plasma velocity using the Halley SuperDARN radar. *Nonlinear Processes in Geophysics*, *14*(6), 799–809. https://doi.org/10.5194/npg-14-799-2007

André, R., Pinnock, M., Villain, J.-P., & Hanuise, C. (2000). On the factor conditioning the Doppler spectral width determined from SuperDARN HF radars. *International Journal of Geomagnetism and Aeronomy*, *2*, 77–86.

Basu, S., Basu, S., MacKenzie, E., Fougere, P. F., Coley, W. R., Maynard, N. C., et al. (1988). Simultaneous density and electric field fluctuation spectra associated with velocity shears in the auroral oval. *Journal of Geophysical Research*, *93*(A1), 115–136. https://doi.org/10.1029/ja093ia01p00115

Billett, D. D., Grocott, A., Wild, J. A., Walach, M.-T., & Kosch, M. J. (2018). Diurnal variations in global Joule heating morphology and magnitude due to neutral winds. *Journal of Geophysical Research*, *123*(3), 2398–2411. https://doi.org/10.1002/2017JA025141

Bruinsma, S., Dudok de Wit, T., Fuller-Rowell, T., Garcia-Sage, K., Mehta, P., Schiemenz, F., et al. (2023). Thermosphere and satellite drag. *Advances in Space Research*. https://doi.org/10.1016/j.asr.2023.05.011

Burlaga, L. F., Vinas, A. F., & Wang, C. (2007). Tsallis distributions of magnetic field strength variations in the heliosphere: 5 to 90 AU. *Journal of Geophysical Research*, *112*(A7), A07206. https://doi.org/10.1029/2006JA012213

Carlson, H. C., Pedersen, T., Basu, S., Keskinen, M., & Moen, J. (2007). Case for a new process, not mechanism, for cusp irregularity production. *Journal of Geophysical Research*, *112*(A11), A11304. https://doi.org/10.1029/2007ja012384

Chaston, C. C., Salem, C., Bonnell, J. W., Carlson, C. W., Ergun, R. E., Strangeway, R. J., & McFadden, J. P. (2008). The turbulent Alfvénic aurora. *Physical Review Letters*, *100*(17), 175003. https://doi.org/10.1103/physrevlett.100.175003

Chisham, G. (2017). A new methodology for the development of high-latitude ionospheric climatologies and empirical models. *Journal of Geophysical Research*, *122*(1), 932–947. https://doi.org/10.1002/2016JA023235

Chisham, G. (2023). Ionospheric vorticity across the northern hemisphere ionosphere determined from particular superdarn radar pairs - 2000 to 2005 inclusive (version 1.0). [dataset]. NERC EDS UK Polar Data Centre. https://doi.org/10.5285/8EEDC594-730B-4AAD-B9CE-827912320C3A

Chisham, G., & Freeman, M. P. (2010). On the non-Gaussian nature of ionospheric vorticity. *Geophysical Research Letters*, *37*(12), L12103. https://doi.org/10.1029/2010GL043714

Chisham, G., & Freeman, M. P. (2021). A statistical model of vorticity in the polar ionosphere and implications for extreme values. *Journal of Geophysical Research*, *126*(11), e2021JA029307. https://doi.org/10.1029/2021JA029307

Chisham, G., & Freeman, M. P. (2023). Separating contributions to plasma vorticity in the high-latitude ionosphere from large-scale convection and meso-scale turbulence. *Journal of Geophysical Research*, *128*(9), e2023JA031885. https://doi.org/10.1029/2023JA031885

Chisham, G., Freeman, M. P., Abel, G. A., Bristow, W. A., Marchaudon, A., Ruohoniemi, J. M., & Sofko, G. J. (2009). Spatial distribution of average vorticity in the high-latitude ionosphere and its variation with interplanetary magnetic field direction and season. *Journal of Geophysical Research*, *114*(A9), A09301. https://doi.org/10.1029/2009JA014263

Chisham, G., Freeman, M. P., Abel, G. A., Lam, M. M., Pinnock, M., Coleman, I. J., et al. (2008). Remote sensing of the spatial and temporal structure of magnetopause and magnetotail reconnection from the ionosphere. *Review of Geophysics*, *46*(1), RG1004. https://doi.org/10.1029/2007RG000223

Chisham, G., Lester, M., Milan, S. E., Freeman, M. P., Bristow, W. A., Grocott, A., et al. (2007). A decade of the super dual auroral radar network (SuperDARN): Scientific achievements, new techniques and future directions. *Surveys in Geophysics*, *28*(1), 33–109. https://doi.org/10.1007/s10712-007-9017-8

Chisham, G., Pinnock, M., & Rodger, A. S. (2000). Poleward-moving HF radar flow bursts in the cusp: Transient changes in flow speed or direction? *Geophysical Research Letters*, *27*(7), 919–922. https://doi.org/10.1029/1999gl010760

Chorin, A. J. (2013). *Vorticity and turbulence* (Vol. 103). Springer Science and Business Media.

Clausen, L. B. N., Baker, J. B. H., Ruohoniemi, J. M., Greenwald, R. A., Thomas, E. G., Shepherd, S. G., et al. (2012). Large-scale observations of a subauroral polarization stream by midlatitude SuperDARN radars: Instantaneous longitudinal velocity variations. *Journal of Geophysical Research*, *117*(A5), A05306. https://doi.org/10.1029/2011ja017232

Cowley, S. W. H., & Lockwood, M. (1992). Excitation and decay of solar wind-driven flows in the magnetosphere-ionosphere system. *Annals of Geophysics*, *10*, 103–115.

Coxon, J. C., Chisham, G., Freeman, M. P., Anderson, B. J., & Fear, R. C. (2022). Distributions of Birkeland current density observed by AMPERE are heavy-tailed or long-tailed. *Journal of Geophysical Research*, *127*(2), e2021JA029801. https://doi.org/10.1029/2021JA029801

Coxon, J. C., Chisham, G., Freeman, M. P., Forsyth, C., Walach, M.-T., Murphy, K. R., et al. (2023). Extreme Birkeland currents are more likely during geomagnetic storms on the dayside of the Earth. *Journal of Geophysical Research*, *128*(12), e2023JA031946. https://doi.org/10.1029/2023JA031946

Di Mare, F., Spicher, A., Clausen, L. B. N., Miloch, W. J., & Moen, J. I. (2021). Turbulence and intermittency in the winter cusp ionosphere studied with the ICI sounding rockets. *Journal of Geophysical Research*, *126*(8), e2021JA029150. https://doi.org/10.1029/2021JA029150

Dungey, J. W. (1961). Interplanetary magnetic field and the auroral zones. *Physical Review Letters*, *6*(2), 47–48. https://doi.org/10.1103/physrevlett.6.47

Eriksen, N. K., Lorentzen, D. A., Oksavik, K., Baddeley, L., Hosokawa, K., Shiokawa, K., et al. (2023). On the creation, depletion, and end of life of polar cap patches. *Journal of Geophysical Research*, *128*(12), e2023JA031739. https://doi.org/10.1029/2023JA031739

Esquivel, A., & Lazarian, A. (2010). Tsallis statistics as a tool for studying interstellar turbulence. *The Astrophysical Journal*, *710*(1), 125–132. https://doi.org/10.1088/0004-637x/710/1/125

Fæhn Follestad, A., Clausen, L. B. N., Thomas, E., Jin, Y., & Coster, A. (2019). Polar cap patch prediction in the expanding contracting polar cap paradigm. *Space Weather*, *17*(11), 1570–1583. https://doi.org/10.1029/2019sw002276

Fedrizzi, M., Fuller-Rowell, T. J., & Codrescu, M. V. (2012). Global Joule heating index derived from thermospheric density physics-based modeling and observations. *Space Weather*, *10*(3), S03001. https://doi.org/10.1029/2011SW000724

Förster, M., Paschmann, G., Haaland, S. E., Quinn, J. M., Torbert, R. B., Vaith, H., & Kletzing, C. A. (2007). High-latitude plasma convection from Cluster EDI measurements: Variances and solar wind correlations. *Annals of Geophysics*, *25*(7), 1691–1707. https://doi.org/10.5194/angeo-25-1691-2007

Foster, J. C. (1983). An empirical electric field model derived from Chatanika radar data. *Journal of Geophysical Research*, *88*(A2), 981–987. https://doi.org/10.1029/ja088ia02p00981

Friis-Christensen, E., McHenry, M. A., Clauer, C. R., & Vennerstrøm, S. (1988). Ionospheric traveling convection vortices observed near the polar cleft: A triggered response to sudden changes in the solar wind. *Geophysical Research Letters*, *15*(3), 253–256. https://doi.org/10.1029/gl015i003p00253

Frisch, U. (2010). *Turbulence: The legacy of A. N. Kolmorgorov*. Cambridge University Press.

Glassmeier, K.-H., & Heppner, C. (1992). Traveling magnetospheric convection twin vortices: Another case study, global characteristics, and a model. *Journal of Geophysical Research*, *97*(A4), 3977–3992. https://doi.org/10.1029/91ja02464

Greenwald, R. A., Baker, K. B., Dudeney, J. R., Pinnock, M., Jones, T. B., Thomas, E. C., et al. (1995). DARN/Superdarn: A global view of the dynamics of high-latitude convection. *Space Science Reviews*, *71*(1–4), 761–796. https://doi.org/10.1007/bf00751350

Greenwald, R. A., Baker, K. B., Hutchins, R. A., & Hanuise, C. (1985). An HF phased-array radar for studying small-scale structure in the high-latitude ionosphere. *Radio Science*, *20*(1), 63–79. https://doi.org/10.1029/rs020i001p00063

Hairston, M. R., & Heelis, R. A. (1990). Model of the high-latitude ionospheric convection pattern during southward interplanetary magnetic field using DE-2 data. *Journal of Geophysical Research*, *95*(A3), 2333–2343. https://doi.org/10.1029/ja095ia03p02333

Heppner, J. P., & Maynard, N. C. (1987). Empirical high-latitude electric field models. *Journal of Geophysical Research*, *92*(A5), 4467–4489. https://doi.org/10.1029/ja092ia05p04467

Hubert, B., Milan, S. E., Grocott, A., Blockx, C., Cowley, S. W. H., & Gerard, J.-C. (2006). Dayside and nightside reconnection rates inferred from IMAGE-FUV and super dual auroral radar network data. *Journal of Geophysical Research*, *111*(A3), A03217. https://doi.org/10.1029/2005ja011140

Kalafatoglu Eyiguler, E. C., Kaymaz, Z., Frissell, N. A., Ruohoniemi, J. M., & Rastätter, L. (2018). Investigating upper atmospheric Joule heating using cross-combination of data for two moderate substorm cases. *Space Weather*, *16*(8), 987–1012. https://doi.org/10.1029/2018sw001956

Kintner, P. M., & Seyler, C. E. (1985). The status of observations and theory of high latitude ionospheric and magnetospheric plasma turbulence. *Space Science Reviews*, *41*(1–2), 91–129. https://doi.org/10.1007/bf00241347

Lam, M. M., Shore, R. M., Chisham, G., Freeman, M. P., Grocott, A., Walach, M.-T., & Orr, L. (2023). A model of high latitude ionospheric convection derived from SuperDARN EOF model data. *Space Weather*, *21*(7), e2023SW003428. https://doi.org/10.1029/2023SW003428

Liu, H.-L., Bardeen, C. G., Foster, B. T., Lauritzen, P., Liu, J., Lu, G., et al. (2018). Development and validation of the whole atmosphere community climate model with thermosphere and ionosphere extension (WACCM-X 2.0). *Journal of Advances in Modeling Earth Systems*, *10*(2), 381–402. https://doi.org/10.1002/2017MS001232

Lockwood, M., Cowley, S. W. H., & Freeman, M. P. (1990). The excitation of plasma convection in the high-latitude ionosphere. *Journal of Geophysical Research*, *95*(A6), 7961–7972. https://doi.org/10.1029/ja095ia06p07961

Lyatsky, W. B., Sofko, G. J., Kustov, A. V., Andre, D., Hughes, W. J., & Murr, D. (1999). Traveling convection vortices as seen by the SuperDARN HF radars. *Journal of Geophysical Research*, *104*(A2), 2591–2601. https://doi.org/10.1029/1998ja900007

Milan, S. E., Gosling, J. S., & Hubert, B. (2012). Relationship between interplanetary parameters and the magnetopause reconnection rate quantified from observations of the expanding polar cap. *Journal of Geophysical Research*, *117*(A3), A03226. https://doi.org/10.1029/2011JA017082

Milan, S. E., Lester, M., Cowley, S. W. H., & Brittnacher, M. (2000). Convection and auroral response to a southward turning of the IMF: Polar UVI, CUTLASS, and IMAGE signatures of transient magnetic flux transfer at the magnetopause. *Journal of Geophysical Research*, *105*(A7), 15741–15755. https://doi.org/10.1029/2000ja900022

Milan, S. E., Lester, M., Cowley, S. W. H., Oksavik, K., Brittnacher, M., Greenwald, R. A., et al. (2003). Variations in the polar cap area during two substorm cycles. *Annals of Geophysics*, *21*(5), 1121–1140. https://doi.org/10.5194/angeo-21-1121-2003

Moen, J., Rinne, Y., Carlson, H. C., Oksavik, K., Fujii, R., & Opgenoorth, H. (2008). On the relationship between thin Birkeland current arcs and reversed flow channels in the winter cusp/cleft ionosphere. *Journal of Geophysical Research*, *113*(A9), A09220. https://doi.org/10.1029/2008ja013061

Moretto, T., & Yahnin, A. (1998). Mapping travelling convection vortex events with respect to energetic particle boundaries. *Annales Geophysicae*, *16*(8), 891–899. https://doi.org/10.1007/s005850050659

Nishimura, Y., Lyons, L. R., Zou, Y., Oksavik, K., Moen, J. I., Clausen, L. B., et al. (2014). Day-night coupling by a localized flow channel visualized by polar cap patch propagation. *Geophysical Research Letters*, *41*(11), 3701–3709. https://doi.org/10.1002/2014GL060301

Nishitani, N., Ruohoniemi, J. M., Lester, M., Baker, J. B. H., Koustov, A. V., Shepherd, S. G., et al. (2019). Review of the accomplishments of mid-latitude super dual auroral radar network (SuperDARN) HF radars. *Progress in Earth and Planetary Science*, *6*(1), 27. https://doi.org/10.1186/s40645-019-0270-5

Oksavik, K., Moen, J., & Carlson, H. C. (2004). High-resolution observations of the small-scale flow pattern associated with a poleward moving auroral form in the cusp. *Geophysical Research Letters*, *31*(11), L11807. https://doi.org/10.1029/2004gl019838

Oksavik, K., Moen, J. I., Rekaa, E. H., Carlson, H. C., & Lester, M. (2011). Reversed flow events in the cusp ionosphere detected by SuperDARN HF radars. *Journal of Geophysical Research*, *116*(A12), A12303. https://doi.org/10.1029/2011ja016788

Orr, L., Grocott, A., Walach, M.-T., Chisham, G., Freeman, M. P., Lam, M. M., & Shore, R. M. (2023). A quantitative comparison of high latitude electric field models during a large geomagnetic storm. *Space Weather*, *21*(1), e2022SW003301. https://doi.org/10.1029/2022SW003301

Pettigrew, E. D., Shepherd, S. G., & Ruohoniemi, J. M. (2010). Climatological patterns of high-latitude convection in the Northern and Southern hemispheres: Dipole tilt dependencies and interhemispheric comparisons. *Journal of Geophysical Research*, *115*(A7), A07305. https://doi.org/10.1029/2009ja014956

Pinnock, M., Rodger, A. S., Dudeney, J. R., Baker, K. B., Newell, P. T., Greenwald, R. A., & Greenspan, M. E. (1993). Observations of an enhanced convection channel in the cusp ionosphere. *Journal of Geophysical Research*, *98*(A3), 3767–3776. https://doi.org/10.1029/92ja01382

Provan, G., Yeoman, T. K., & Milan, S. E. (1998). CUTLASS Finland radar observations of the ionospheric signatures of flux transfer events and the resulting plasma flows. *Annales Geophysicae*, *16*(11), 1411–1422. https://doi.org/10.1007/s005850050707

Qiao, H. Z., & Tsokos, C. P. (1994). Parameter estimation of the Weibull probability distribution. *Mathematics and Computers in Simulation*, *37*(1), 47–55. https://doi.org/10.1016/0378-4754(94)90058-2

Ridley, A. J., Crowley, G., & Freitas, C. (2000). An empirical model of the ionospheric electric potential. *Geophysical Research Letters*, *27*(22), 3675–3678. https://doi.org/10.1029/1999gl011161

Rinne, Y., Moen, J., Oksavik, K., & Carlson, H. C. (2007). Reversed flow events in the winter cusp ionosphere observed by the European Incoherent Scatter (EISCAT) Svalbard radar. *Journal of Geophysical Research*, *112*(A10), A10313. https://doi.org/10.1029/2007ja012366

Ruohoniemi, J. M., & Baker, K. B. (1998). Large-scale imaging of high-latitude convection with super dual auroral radar network HF radar observations. *Journal of Geophysical Research*, *103*(A9), 20797–20811. https://doi.org/10.1029/98ja01288

Ruohoniemi, J. M., & Greenwald, R. A. (2005). Dependencies of high-latitude plasma convection: Consideration of interplanetary magnetic field, seasonal, and universal time factors in statistical patterns. *Journal of Geophysical Research*, *110*(A9), A09204. https://doi.org/10.1029/2004ja010815

Russell, C. T., & Elphic, R. C. (1979). ISEE observations of flux transfer events at the dayside magnetopause. *Geophysical Research Letters*, *6*(1), 33–36. https://doi.org/10.1029/gl006i001p00033

Sandholt, P. E., Lockwood, M., Oguti, T., Cowley, S. W. H., Freeman, K. S. C., Lybekk, B., et al. (1990). Midday auroral breakup events and related energy and momentum transfer from the magnetosheath. *Journal of Geophysical Research*, *95*(A2), 1039–1060. https://doi.org/10.1029/ja095ia02p01039

Sangha, H., Milan, S. E., Carter, J. A., Fogg, A. R., Anderson, B. J., Korth, H., & Paxton, L. J. (2020). Bifurcated region 2 field-aligned currents associated with substorms. *Journal of Geophysical Research*, *125*(1), e2019JA027041. https://doi.org/10.1029/2019ja027041

Shalizi, C. R. (2007). Maximum likelihood estimation for q-exponential (Tsallis) distributions. Retrieved from arXiv:math/0701854v2

Shepherd, S. G. (2014). Altitude-adjusted corrected geomagnetic coordinates: Definition and functional approximations. *Journal of Geophysical Research*, *119*(9), 7501–7521. https://doi.org/10.1002/2014JA020264

Shore, R. M., Freeman, M. P., & Chisham, G. (2021). Data-driven basis functions for SuperDARN ionospheric plasma flow characterization and prediction. *Journal of Geophysical Research*, *126*(7), e2021JA029272. https://doi.org/10.1029/2021JA029272

Siscoe, G. L., & Huang, T. S. (1985). Polar cap inflation and deflation. *Journal of Geophysical Research*, *90*(A1), 543–547. https://doi.org/10.1029/ja090ia01p00543

Sofko, G. J., Greenwald, R. A., & Bristow, W. (1995). Direct determination of large-scale magnetospheric field-aligned currents with SuperDARN. *Geophysical Research Letters*, *22*(15), 2041–2044. https://doi.org/10.1029/95gl01317

Spicher, A., Ilyasov, A. A., Miloch, W. J., Chernyshov, A. A., Clausen, L. B. N., Moen, J. I., et al. (2016). Reverse flow events and small-scale effects in the cusp ionosphere. *Journal of Geophysical Research: Space Physics*, *121*(10), 10466–10480. https://doi.org/10.1002/2016ja022999

Spicher, A., LaBelle, J., Bonnell, J. W., Roglans, R., Moser, C., Fuselier, S. A., et al. (2022). Interferometric study of ionospheric plasma irregularities in regions of phase scintillations and HF backscatter. *Geophysical Research Letters*, *49*(12), e2021GL097013. https://doi.org/10.1029/2021GL097013

Spicher, A., Miloch, W. J., Clausen, L. B. N., & Moen, J. I. (2015). Plasma turbulence and coherent structures in the polar cap observed by the ICI-2 sounding rocket. *Journal of Geophysical Research*, *120*(12), 10959–10978. https://doi.org/10.1002/2015ja021634

Thomas, E. G., & Shepherd, S. G. (2018). Statistical patterns of ionospheric convection derived from mid-latitude, high-latitude, and polar SuperDARN HF radar observations. *Journal of Geophysical Research*, *123*(4), 3196–3216. https://doi.org/10.1002/2018ja025280

Vallières, X., Villain, J.-P., Hanuise, C., & André, R. (2004). Ionospheric propagation effects on spectral widths measured by SuperDARN HF radars. *Annals of Geophysics*, *22*(6), 2023–2031. https://doi.org/10.5194/angeo-22-2023-2004

van der Meeren, C., Oksavik, K., Lorentzen, D. A., Rietveld, M. T., & Clausen, L. B. N. (2015). Severe and localized GNSS scintillation at the poleward edge of the nightside auroral oval during intense substorm aurora. *Journal of Geophysical Research: Space Physics*, *120*(12), 10607–10621. https://doi.org/10.1002/2015JA021819

Villain, J.-P., André, R., Pinnock, M., Greenwald, R. A., & Hanuise, C. (2002). A statistical study of the Doppler spectral width of high-latitude ionospheric F-region echoes recorded with SuperDARN coherent HF radars. *Annales Geophysicae*, *20*(11), 1769–1781. https://doi.org/10.5194/angeo-20-1769-2002

Villain, J.-P., Hanuise, C., & Caudal, G. (1985). A SAFARI-EISCAT comparison between the velocity of F region small-scale irregularities and the ion drift. *Journal of Geophysical Research*, *90*(A9), 8433–8443. https://doi.org/10.1029/ja090ia09p08433

Weimer, D. R. (2001). An improved model of ionospheric electric potentials including substorm perturbations and application to the geospace environment modeling november 24 1996 event. *Journal of Geophysical Research*, *106*(A1), 407–416. https://doi.org/10.1029/2000ja000604

Weimer, D. R. (2005). Improved ionospheric electrodynamic models and application to calculating Joule heating rates. *Journal of Geophysical Research*, *110*(A5), A05306. https://doi.org/10.1029/2004JA010884

Wild, J. A., Yeoman, T. K., Eglitis, P., & Opgenoorth, H. J. (2000). Multi-instrument observations of the electric and magnetic field structure of omega bands. *Annales Geophysicae*, *18*(1), 99–110. https://doi.org/10.1007/s00585-000-0099-6

Zhang, Q.-H., Ma, Y.-Z., Jayachandran, P. T., Moen, J., Lockwood, M., Zhang, Y.-L., et al. (2017). Polar cap hot patches: Enhanced density structures different from the classical patches in the ionosphere. *Geophysical Research Letters*, *44*(16), 8159–8167. https://doi.org/10.1002/2017GL073439

Zhang, Q.-H., Zhang, B.-C., Lockwood, M., Hu, H.-Q., Moen, J., Ruohoniemi, J. M., et al. (2013). Direct observations of the evolution of polar cap ionization patches. *Science*, *339*(6127), 1597–1600. https://doi.org/10.1126/science.1231487